

# Jet Evolution and the Underlying Event in Proton-Antiproton Collisions at 1.8 TeV

Rick Field and David Stuart for the CDF Collaboration

January 1, 2000

## Abstract

The growth and development of “charged particle jets” produced in proton-antiproton collisions at 1.8 TeV are studied. A variety of “local” leading jet observables are compared with the QCD “hard scattering” Monte-Carlo models of Herwig, Isajet, and Pythia. The models describe quite well (*although not completely*) the multiplicity distribution of charged particles within the leading jet, the “size” of the leading jet, the radial flow of charged particles and transverse momentum around the leading jet direction, and the momentum distribution of charged particles within the leading jet. Also, a number of “global” observables are examined, where to fit the observable the QCD Monte-Carlo models have to describe correctly the entire proton-antiproton event structure. In particular, we study carefully the growth and structure of the “underlying event” in hard scattering processes. None of the models (*with their default parameters*) describe correctly all the properties of the underlying event.

## I. Introduction

The total proton-antiproton cross section is the sum of the elastic and inelastic cross sections. The inelastic cross section consists of a single-diffractive, double-diffractive, and a “hard core” component. The “hard core” component is everything non-diffractive. It is what is left after one removes the single-diffractive and the double-diffractive events. “Hard core”, of course, does not necessarily imply “hard scattering”. A “hard scattering” collision, such as that illustrated in Fig. 1.1, is one in which a “hard” (*i.e.* large transverse momentum) 2-to-2 parton-parton subprocess has occurred. “Soft” hard core collisions correspond to events in which no “hard” interaction has occurred. When there is no large transverse momentum subprocess in the collision one is not probing short distance and it probably does not make any sense to talk about partons. The QCD “hard scattering” cross section grows with increasing collider energy. As the center-of-mass energy of a proton-antiproton collision increases, “hard” scattering becomes a larger and larger fraction of the total inelastic cross section. Here we use our Min-Bias trigger data sample in conjunction with our JET20 trigger data sample to study the growth and development of “charged particle jets” from  $P_T(\text{jet}) = 0.5$  to 50 GeV. We compare a variety of “local” jet observables with the QCD “hard scattering” Monte-Carlo models of Herwig [1], Isajet [2], and Pythia [3].

A “hard scattering” event, like that illustrated in Fig. 1.1 consists of large transverse momentum outgoing hadrons that originate from the large transverse momentum partons (*i.e.* outgoing hard scattering jets) and also hadrons that originate from the break-up of the proton and antiproton (*i.e.* the “beam-beam remnants”). The “underlying event” is an interesting object that is not very well understood. In addition to beam-beam remnants, it may contain hadrons resulting from initial-state radiation. Also, it is possible that multiple parton scattering occurs in

hadron-hadron collisions as illustrated in Fig. 1.2. This is a controversial issue, but the underlying event might also contains hadrons that originate from multiple parton interactions. Pythia, for example, uses multiple parton interactions as a way to enhance the activity of the underlying event [3].

In addition to studying “local” leading jet observables, we study a variety of “global” observables, where to fit the observable the QCD Monte-Carlo models have to describe correctly the entire proton-antiproton event structure. We examine closely the growth and structure of the underlying event. We find that the underlying “hard scattering” event is not the same as a “soft” proton-antiproton collision. For the same available energy the underlying event in a hard scattering is considerable more active (*i.e.* higher charge particle density and more transverse momentum) than a “soft” collision. This is not surprising since a violent hard scattering has occurred! We find that none of the QCD Monte-Carlo models (*with their default parameters*) describe correctly all the properties of the underlying event. For example, none of the models produce the correct  $P_T$  dependence of the beam-beam remnant contribution to the underlying event.

In Section II we discuss the data and the QCD Monte-Carlo models used in this analysis and we explain the procedure used to compare theory with data. In Section III, we define “charge particle jets” as simple circular regions in  $\eta$ - $\phi$  space with  $R = 0.7$  and watch the growth and development of these “jets” from 0.5 to 50 GeV. In Section IV, we study a variety of “global” observables, where to fit the observable the QCD Monte-Carlo models have to describe correctly the entire proton-antiproton event. The structure of the underlying event is examined in Section V and we reserve Section VI for summary and conclusions.

## II. Data Selection and Monte-Carlo Models

### (1) Data Selection

The CDF detector, described in detail in Ref. [4], measures the trajectories and transverse momenta,  $P_T$ , of charged particles in the pseudorapidity region  $|\eta| < 1.1$  with the central tracking chamber (CTC), silicon vertex detector (SVX), and vertex time projection chamber (VTX), which are immersed in a 1.4 T solenoidal magnetic field. In this analysis we consider only charged particles measured in the central tracking chamber (CTC) and use the two trigger sets of data listed in Table 1. The minimum bias (min-bias) data were selected by requiring at least one particle interact with the forward beam-beam counter BBC ( $3.4 < \eta < 5.9$ ) *and* at least one particle interact with the backward BBC ( $-5.9 < \eta < -3.4$ ). The min-bias trigger selects predominately the “hard core” component of the inelastic cross section.

Charged particle tracks are found with high efficiency as long as the density of particles is not high. To remain in a region of high efficiency, we consider only charged particles with  $P_T > 0.5$  GeV and  $|\eta| < 1$ . The observed tracks include some fake tracks that result from secondary interactions between primary particles, including neutral particles, and the detector material. There are also particles originating from other proton-antiproton collisions. To reduce the contribution from these sources, we consider only tracks which point to the primary interaction vertex within 2 cm along the beam direction and 1 cm transverse to the beam direction. Detector

simulations indicate that this impact parameter cut is very efficient and that the number of fake tracks is about 3.5% when a 1 cm impact parameter cut is applied in conjunction with a 2 cm vertex cut. Without the impact parameter cut the number of fake tracks is approximately 9%.

This dependence of the number of fake tracks on the CTC impact parameter cut provides a method of estimating systematic uncertainties due to fakes. Every data point,  $P$ , on every plot in this analysis was determined three times by using a 2 cm vertex cut in conjunction with three different CTC  $d_0$  cuts; a 1 cm CTC  $d_0$  cut ( $P$ ), a 0.5 cm CTC  $d_0$  cut ( $P_1$ ), and no CTC  $d_0$  cut ( $P_2$ ). The 1 cm cut determined the value of the data point,  $P$ , and the difference between the 0.5 cm cut value and no cut value of the data point determined the systematic error of the data point as follows:  $\text{sys-error} = P|P_2 - P_1|/P_1$ . This systematic error was then added in quadrature with the statistical error. We do not correct the data for the CTC track finding efficiency. Instead the theoretical Monte-Carlo model predictions are corrected for the track finding efficiency.

**Table 1.** Data sets and selection criterion used in this analysis.

CDF Data Set	Trigger	Events	Selection
Min-Bias	Min-Bias Trigger	626,966	zero or one vertex in $ z  < 100$ cm $ z_c - z_v  < 2$ cm, $ \text{CTC } d_0  < 1$ cm $P_T > 0.5$ GeV, $ \eta  < 1$
JET20	Calorimeter tower cluster with $E_T > 20$ GeV	78,682	zero or one vertex in $ z  < 100$ cm $ z_c - z_v  < 2$ cm, $ \text{CTC } d_0  < 1$ cm $P_T > 0.5$ GeV, $ \eta  < 1$

## (2) QCD “Hard Scattering” Monte-Carlo Models

The “hard” scattering QCD Monte-Carlo models used in this analysis are listed in Table 2. The QCD perturbative 2-to-2 parton-parton differential cross section diverges as the transverse momentum of the scattering,  $PT(\text{hard})$ , goes to zero (see Fig. 1.1). One must set a minimum  $PT(\text{hard})$  large enough so that the resulting cross section is not larger than the total “hard core” inelastic cross section, and also large enough to ensure that QCD perturbation theory is applicable. In this analysis we take  $PT(\text{hard}) > 3$  GeV.

**Table 2.** Theoretical QCD “hard” scattering Monte-Carlo models studied in this analysis. In all cases we take  $PT(\text{hard}) > 3$  GeV.

Monte-Carlo Model	Subprocesses	Comments
Herwig 5.9	QCD 2-to-2 parton scattering: IPROC = 1500	Default values for all parameters
Isajet 7.32	QCD 2-to-2 parton scattering: TWOJET	Default values for all parameters
Pythia 6.115	QCD 2-to-2 parton scattering: MSEL = 1	Default values for all parameters: PARP(81) = 1.4
Pythia 6.125	QCD 2-to-2 parton scattering: MSEL = 1	Default values for all parameters: PARP(81) = 1.9
Pythia No MS	QCD 2-to-2 parton scattering: MSEL = 1	Pythia 6.125 with no multiple parton interactions: MSTP(81) = 0

Each of the QCD Monte-Carlo models handle the “beam-beam remnants” (Fig. 1.1) in a similar fashion. A hard scattering event is basically the superposition of a hard parton-parton interaction on top of a “soft” collision. Herwig [1] assumes that the underlying event is a soft collision between the two “beam clusters”. Isajet [2] uses a model similar to the one it uses for soft “min-bias” events (*i.e.* “cut Pomeron”), but with different parameters, to describe the underlying beam-beam remnants. Pythia [3] assumes that each incoming beam hadron leaves behind a “beam remnant”, which do not radiate initial state radiation, and simply sail through unaffected by the hard process. However, unlike Herwig and Isajet, Pythia also uses multiple parton interactions to enhance the activity of the underlying event as illustrated in Fig. 1.2.

In this analysis we examine two versions of Pythia, Pythia 6.115 and Pythia 6.125 both with the default values for all the parameters. The default values of the parameters are different in version 6.115 and 6.125. In particular, the effective minimum transverse momentum for multiple parton interactions, PARP(81), changed from 1.4 GeV in version 6.115 to 1.9 GeV in version 6.125. Increasing this cut-off decreases the multiple parton interaction cross section which reduces the amount of multiple parton scattering. For completeness, we also consider Pythia with no multiple parton scattering (MSTP(81)=0).

Since Isajet employs “independent fragmentation” it is possible to trace particles back to their origin and divide them into three categories: particles that arise from the break-up of the beam and target (*beam-beam remnants*), particles that arise from initial-state radiation, and particles that result from the outgoing hard scattering jets plus final-state radiation. The “hard scattering component” consists of the particles that arise from the outgoing hard scattering jets plus initial and final-state radiation (*sum of the last two categories*). Particles from the first two categories (*beam-beam remnants plus initial-state radiation*) are normally what is referred to as the underlying event (see Fig 1.1). Of course, these categories are not directly observable experimentally. Nevertheless, it is instructive to examine how particles from various origins affect the experimental observables.

Since Herwig and Pythia do not use independent fragmentation, it is not possible to distinguish particles that arise from initial-state radiation from those that arise from final-state radiation, but we can identify the beam-beam remnants. When, for example, a color string breaks into hadrons it is not possible to say which of the two partons producing the string was the parent. For Herwig and Pythia we divide particles into two categories: particles that arise from the break-up of the beam and target (*beam-beam remnants*), and particles that result from the outgoing hard scattering jets plus initial and final-state radiation (*hard scattering component*). For Pythia we include particles that arise from multiple parton interactions in the beam-beam remnant component.

### (3) Method of Comparing Theory with Data

Our philosophy in comparing the theory with data in this analysis is to select a region where the data is very “clean”. The CTC efficiency can vary substantially for very low  $P_T$  tracks and in dense high  $P_T$  jets. To avoid this we have considered only the region  $P_T > 0.5$  GeV and  $|\eta| < 1$  where the CTC efficiency is high and stable (estimated to be 92% efficient) and we restrict ourselves to jets less than 50 GeV. The data presented here are uncorrected. Instead the theoretical Monte-Carlo predictions are corrected for the track finding efficiency and have an

error (*statistical plus systematic*) of about 5%. The errors on the (*uncorrected*) data include both statistical and correlated systematic uncertainties.

In comparing the QCD “hard scattering” Monte-Carlo models with the data, we require that the Monte-Carlo events satisfy the CDF min-bias trigger and we apply an 8% correction for the CTC track finding efficiency. The corrections are small. On the average, 8 out of every 100 charged particles predicted by the theory are removed from consideration. Requiring the theory to satisfy the min-bias trigger is important when comparing with the Min-Bias data, but does not matter when comparing with the JET20 data since essentially all high  $P_T$  jet events satisfy the min-bias trigger.

### III. The Evolution of Charge Particle “Jets” from 0.5 to 50 GeV

In this section, we define charged particle “jets” and examine the evolution of these “jets” from  $P_{T(\text{jet})} = 0.5$  to 50 GeV. As illustrated in Fig. 3.1, “jets” are defined as “circular regions” ( $R = 0.7$ ) in  $\eta$ - $\phi$  space and contain charged particles from the underlying event as well as particles which originate from the fragmentation of high  $P_T$  outgoing partons (see Fig 1.1). Also every charged particle in the event is assigned to a “jet”, with the possibility that some “jets” might consist of just one charged particle. We adapt a very simple jet definition since we will be dealing with “jets” that consist of only a few low  $P_T$  charged particles. The standard jet algorithm based on calorimeter clustering is not applicable at low transverse momentum.

#### (1) Jet Definition (charged particles)

We define jets as circular regions in  $\eta$ - $\phi$  space with “distance” defined by

$$R = \sqrt{(\Delta\eta)^2 + (\Delta\phi)^2}.$$

Our jet algorithm is as follows:

- Order all charged particles according to their  $P_T$ .
- Start with the highest  $P_T$  particle and include in the “jet” all particles within the “radius”  $R = 0.7$ .
- Go to the next highest  $P_T$  particle (*not already included in a “jet”*) and add to the “jet” all particles (*not already included in a “jet”*) within  $R = 0.7$ .
- Continue until all particles are in a “jet”.

We consider all charged particles ( $P_T > 0.5$  GeV and  $|\eta| < 1$ ) and allow the jet radius to extend outside  $|\eta| < 1$ . Fig. 3.1 illustrates an event with six charged particles and five jets. We define the transverse momentum of the “jet” to be the *scalar*  $P_T$  sum of all the particles within the “jet” (*i.e.* it is simply the *scalar*  $P_T$  sum within the circular region).

The maximum number of jets is related to the geometrical size of jets compared to the size of the region considered and is given approximately by

$$N_{jet}(\text{max}) \approx 2 \frac{(2)(2\pi)}{\pi(0.7)^2} \approx 16.$$

The additional factor of two is to allow for the overlap of “jet” radii as shown in Fig. 3.1.

We know that the simple charged particle jet definition used here is not theoretically favored since if applied at the parton level it is not infrared safe. Of course, all jet definitions (*and in fact all observables*) are infrared safe at the hadron level. We have done a detailed study comparing the naïve jet definition used here with a variety of more sophisticated charge particle jet definitions. This analysis will be presented in a future publication. Some of the observables presented here do, of course, depend on ones definition of a jet and it is important to apply the same definition to both the theory and data.

## (2) Charged Jet Multiplicity versus $P_T(\text{jet\#1})$

Fig. 3.2 shows the average number of charged particles ( $P_T > 0.5$  GeV and  $|\eta| < 1$ ) within jet#1 (*leading charged jet*) as a function of  $P_T(\text{jet\#1})$ . The solid points are Min-Bias data and the open points are the JET20 data. The JET20 data connect smoothly to the Min-Bias data and allows us to study observables over the range  $0.5 < P_T(\text{jet\#1}) < 50$  GeV. There is a small overlap region where the Min-Bias and JET20 data agree. The errors on the data include both statistical and correlated systematic uncertainties, however, the data have not been corrected for efficiency. Fig. 3.2 shows a sharp rise in the leading charged jet multiplicity at low  $P_T(\text{jet\#1})$  and then a flattening out and a gradual rise at high  $P_T(\text{jet\#1})$ . The data are compared with the QCD “hard scattering” Monte-Carlo predictions of Herwig 5.9, Isajet 7.32, and Pythia 6.115. The theory curves are corrected for the track finding efficiency and have an error (statistical plus systematic) of around 5%.

Fig. 3.3 shows the multiplicity distribution of the charged particles within jet#1 (*leading charged jet*) for  $P_T(\text{jet\#1}) > 2, 5$ , and 30 GeV, respectively. Below 2 GeV the probability that the leading charged jet consists of just one particle becomes large. Charge particle jets are “born” somewhere around  $P_T(\text{jet\#1}) = 2$  GeV with, on average, about 2 charged particles and grow to, on average, about 10 charged particles at 50 GeV. Fig. 3.4 shows the multiplicity distribution of charged particles within jet#1 (*leading charged jet*) for  $P_T(\text{jet\#1}) > 5$  and 30 GeV compared with the QCD “hard scattering” Monte-Carlo predictions of Herwig 5.9, Isajet 7.32, and Pythia 6.115. The Monte-Carlo models agree fairly well with the data at both 5 and 30 GeV.

## (3) Charged Jet “Size” versus $P_T(\text{jet\#1})$

Although the charged particle jets are defined as circular regions in  $\eta$ - $\phi$  space with  $R = 0.7$ , this is not the “size” of the jet. The “size” of a jet can be defined in two ways, size according to particle number and size according to transverse momentum. The first corresponds to the radius in  $\eta$ - $\phi$  space that contains 80% of the charged particles in the jet and the second corresponds to the radius in  $\eta$ - $\phi$  space that contains 80% of the jet transverse momentum. The data on the average “jet size” of the leading charge particle jet are compared with the QCD “hard scattering” Monte-Carlo predictions of Herwig 5.9, Isajet 7.32, and Pythia 6.115 in Fig. 3.5. A leading 20 GeV charged jet has 80% of its charged particles contained, on the average, within a radius in  $\eta$ - $\phi$  space of about 0.33, and 80% of its transverse momentum contained, on the average, within a radius of about 0.20. Fig. 3.5 clearly illustrate the “hot core” of jets. The

radius containing 80% of the transverse momentum is smaller than the radius that contains 80% of the particles. Furthermore, the radius containing 80% of the transverse momentum decreases as the overall transverse momentum of the jet increases due to limited momentum perpendicular to the jet direction.

We can study the radial distribution of charged particles and transverse momentum within the leading jet by examining the distribution of  $\langle N_{\text{chg}} \rangle$  and  $\langle P_{T\text{sum}} \rangle$  as a function of the distance in  $\eta$ - $\phi$  space from the leading jet direction as illustrated in Fig. 3.6. Fig. 3.7 and Fig. 3.8 compare data on the radial multiplicity flow and the radial transverse momentum flow, for  $P_T(\text{jet}\#1) > 5$  and 30 GeV compared with the QCD “hard scattering” Monte-Carlo predictions of Herwig 5.9, Isajet 7.32, and Pythia 6.115. For an “average charged jet” with  $P_T(\text{jet}\#1) > 5$  GeV ( $> 30$  GeV), 80% of the jet  $P_T$  lies within  $R = 0.36$  (0.18). Note that because of the nature of QCD fluctuations the “average jet size” shown in Fig. 3.5 is not exactly the same as the “size of an average jet” shown in Fig. 3.7 and 3.8. A given jet rarely looks like an “average jet” and at low  $P_T(\text{jet}\#1)$  the “average jet size” is slightly smaller than the “size of an average jet”.

#### (4) Momentum Distribution of Charged Particles within Jet#1

We define a “charged jet fragmentation function”,  $F(z)$ , which describes the momentum distribution of charged particles within the leading charged particle jet. The function  $F(z)$  is the number of charged particles between  $z$  and  $z + dz$  (*i.e.* the charge particle number density), where  $z = p/P_{\text{jet}}$  is the fraction of the overall charged particle momentum of the jet carried by the charged particle with momentum  $p$ . The integral of  $F(z)$  over  $z$  is the average multiplicity of charged particles within the jet. We refer to this as a “fragmentation function”, however it is not a *true* fragmentation function since we are dealing only with charged particle jets. Furthermore, some of the charged particles within the leading jets originate from the underlying event and we can never be sure that we have included all the particles that come from the outgoing high transverse momentum parton.

Fig. 3.9 shows the data on  $F(z)$  for  $P_T(\text{jet}\#1) > 2, 5$ , and 30 GeV. The data roughly scale for  $P_T(\text{jet}\#1) > 5$  GeV and  $z > 0.1$ , with the growth in multiplicity coming from the “soft” particles (*i.e.* low  $z$  region). This is exactly the behavior expected from a “fragmentation function”. Fig. 3.10 and Fig. 3.11 compare data on the  $F(z)$  for  $P_T(\text{jet}\#1) > 5$  and 30 GeV, respectively, with the QCD “hard” scattering Monte-Carlo predictions of Herwig 5.9, Isajet 7.32, and Pythia 6.115.

The QCD “hard scattering” models describe quite well the multiplicity distribution of charged particles within the leading jet (Fig. 3.4), the “size” of the leading jet (Fig. 3.5), the radial flow of charged particles and transverse momentum around the leading jet direction (Fig. 3.7 – Fig. 3.8), and the momentum distribution of charged particles within the leading jet (Fig. 3.10 – Fig. 3.11). We now proceed to study the overall event structure as a function of transverse momentum of the leading charged jet.

## IV. The Overall Event Structure as a Function of $P_T(\text{jet}\#1)$

In the previous section we studied “local” leading jets observables. The QCD Monte-Carlo models did not have to describe correctly the entire event in order to fit the observable. They only had to describe correctly the properties of the leading charge particle jet, and all the models fit the data fairly well (*although not perfectly*). Now we will study “global” observables, where to fit the observable the QCD Monte-Carlo models will have to describe correctly the entire event structure.

### (1) Overall Charged Multiplicity versus $P_T(\text{jet}\#1)$

Fig. 4.1 shows the average number of charged particles in the event with  $P_T > 0.5$  GeV and  $|\eta| < 1$  (*including jet#1*) as a function of  $P_T(\text{jet}\#1)$  (*leading charged jet*) for the Min-Bias and JET20 data. Again the JET20 data connect smoothly to the Min-Bias data and there is a small overlap region where the Min-Bias and JET20 data agree. Fig. 4.1 shows a sharp rise in the overall charged multiplicity at low  $P_T(\text{jet}\#1)$  and then a flattening out and a gradual rise at high  $P_T(\text{jet}\#1)$  similar to Fig. 3.2. We would like to investigate where these charged particles are located relative to the direction of the leading charged particle jet.

### (2) Correlations in $\Delta\phi$ relative to $P_T(\text{jet}\#1)$

As illustrated in Fig. 4.2, the angle  $\Delta\phi$  is defined to be the relative azimuthal angle between charged particles and the direction of the leading charged particle jet. Plots of  $\langle N_{\text{chg}} \rangle$  and  $\langle P_{T\text{sum}} \rangle$  as a function of  $\Delta\phi$  are referred to as “charged multiplicity flow in  $\phi$ ” relative to jet#1 and “transverse momentum flow in  $\phi$ ” relative to jet#1, respectively. All charged particles ( $P_T > 0.5$  GeV and  $|\eta| < 1$ ) are included in these plots (*including those in jet#1*). Fig. 4.3 and Fig. 4.4 shows the data on the charged multiplicity flow and transverse momentum flow, respectively, in  $\phi$  relative to the leading charged particle jet for  $P_T(\text{jet}\#1) > 2, 5$ , and 30 GeV.

Fig. 4.5 and Fig. 4.6 compare the data on the charged multiplicity flow and transverse momentum flow in  $\phi$  relative to the leading charged particle jet with the QCD “hard scattering” Monte-Carlo predictions of Herwig 5.9, Isajet 7.32, and Pythia 6.115 for  $P_T(\text{jet}\#1) > 5$  GeV and Fig. 4.7 and Fig. 4.8 for  $P_T(\text{jet}\#1) > 30$  GeV. Here one sees differences in the QCD Monte-Carlo models and they do not agree as well with these “global” observables as they did with “local” leading jet observables.

In Fig. 4.3 and Fig. 4.4 we have labeled the region  $|\phi - \phi_{\text{jet}\#1}| < 60^\circ$  as “toward” jet#1 and the region  $|\phi - \phi_{\text{jet}\#1}| > 120^\circ$  as “away” from jet#1. The “transverse” to jet#1 region is defined by  $60^\circ < |\phi - \phi_{\text{jet}\#1}| < 120^\circ$ . As illustrated in Fig. 4.2, each region, “toward”, “transverse”, and “away” covers the same range  $|\Delta\eta| \times |\Delta\phi| = 2 \times 120^\circ$ . The “toward” region includes the particles from jet#1 as well as a few particles from the underlying event. As we will see, the “transverse” region is very sensitive to the underlying event. The “away” region is a mixture of the

underlying event and the “away-side” hard scattering jet. Fig. 4.3 and 4.4 show a rapid growth in the “toward” and “away” region as  $P_T(\text{jet\#1})$  increases.

Fig. 4.9 shows the data on the average number of charged particles ( $P_T > 0.5$  GeV and  $|\eta| < 1$ ) as a function of  $P_T(\text{jet\#1})$  for the three regions. Each point corresponds to the “toward”, “transverse”, or “away”  $\langle N_{\text{chg}} \rangle$  in a 1 GeV bin. The solid points are Min-Bias data and the open points are JET20 data. The data in Fig. 4.9 define the average event “shape”. For example, for an “average” proton-antiproton collider event at 1.8 TeV with  $P_T(\text{jet\#1}) = 20$  GeV there are, on the average, 8.7 charged particles “toward” jet#1 (*including the particles in jet#1*), 2.5 “transverse” to jet#1, and 4.9 “away” from jet#1.

Fig. 4.10 shows the data on the average *scalar*  $P_T$  sum of charged particles ( $P_T > 0.5$  GeV and  $|\eta| < 1$ ) as a function of  $P_T(\text{jet\#1})$  for the three regions. Each point corresponds to the “toward”, “transverse”, or “away”  $\langle P_{T\text{sum}} \rangle$  in a 1 GeV bin. In Fig. 4.11 data on the  $\langle N_{\text{chg}} \rangle$  as a function of  $P_T(\text{jet\#1})$  for the three regions are compared with the QCD “hard” scattering Monte-Carlo predictions of Herwig 5.9, Isajet 7.32, and Pythia 6.115. The QCD Monte-Carlo models agree qualitatively (*but not precisely*) with the data. We will now examine more closely these three regions.

### (3) The “Toward” and “Away” Region versus $P_T(\text{jet\#1})$

Fig. 4.12 shows the data from Fig.4.9 on the average number of “toward” region charged particles compared with the QCD “hard scattering” Monte-Carlo predictions of Herwig 5.9, Isajet 7.32, and Pythia 6.115. This plot is very similar to the average number of charged particles within the leading jet shown in Fig. 3.2. At  $P_T(\text{jet\#1}) = 20$  GeV the “toward” region contains, on the average, about 8.7 charged particles with about 6.9 of these charged particles belonging to jet#1. As expected the toward region is dominated by the leading jet. This is seen clearly in Fig. 4.13 where the predictions of Isajet for the “toward” region are divided into three categories: charged particles that arise from the break-up of the beam and target (*beam-beam remnants*), charged particles that arise from initial-state radiation, and charged particles that result from the outgoing jets plus final-state radiation. For  $P_T(\text{jet\#1})$  values below 5 GeV the “toward” region charged multiplicity arises mostly from the beam-beam remnants, but as  $P_T(\text{jet\#1})$  increases the contribution from the outgoing jets plus final state-radiation quickly begins to dominate. The bump in the beam-beam remnant contribution at low  $P_T(\text{jet\#1})$  is caused by leading jets composed almost entirely from the remnants.

Fig. 4.14 shows the data from Fig.4.9 on the average number of “away” region charged particles compared with the QCD “hard scattering” Monte-Carlo predictions of Herwig 5.9, Isajet 7.32, and Pythia 6.115. In Fig. 4.15 the data from Fig. 4.10 on the average *scalar*  $P_T$  sum in the “away” region is compared to the QCD Monte-Carlo predictions. The “away” region is a mixture of the underlying event and the “away-side” outgoing “hard scattering” jet. This can be seen in Fig. 4.16 where the predictions of Isajet for the “away” region are divided into three categories: beam-beam remnants, initial-state radiation, and outgoing jets plus final-state radiation. Here the underlying event plays a more important role since the “away-side” outgoing “hard scattering” jet is sometimes outside the regions  $|\eta| < 1$ . For the “toward” region the

contribution from the outgoing jets plus final state-radiation dominates for  $P_{T(\text{jet}\#1)}$  values above about 5 GeV, whereas for the “away” region this does not occur until around 20 GeV.

Both the “toward” and “away” regions are described fairly well by the QCD “hard scattering” Monte-Carlo models. These regions are dominated by the outgoing “hard scattering” jets and as we saw in Section III the Monte-Carlo models describe the leading outgoing jets fairly accurately. We will now study the “transverse” region which is dominated by the underlying event.

## V. The “Transverse” Region and the Underlying Event

Fig. 4.9 shows that there is a lot of activity in the “transverse” region. If we suppose that the “transverse” multiplicity is uniform in azimuthal angle  $\phi$  and pseudo-rapidity  $\eta$ , the observed 2.3 charged particles at  $P_{T(\text{jet}\#1)} = 20$  GeV translates to 3.8 charged particles per unit pseudo-rapidity with  $P_T > 0.5$  GeV (multiply by 3 to get  $360^\circ$ , divide by 2 for the two units of pseudo-rapidity, multiply by 1.09 to correct for the track finding efficiency). We know that if we include all  $P_T$  that there are roughly 4 charged particles per unit rapidity in a “soft” proton-antiproton collision at 1.8 TeV and our data show that in the underlying event of a “hard scattering” there are about 3.8 charged particles per unit rapidity in the region  $P_T > 0.5$  GeV! If one includes all  $P_T$  values then the underlying event has a charge particle density that is at least a factor of two larger than the 4 charged particles per unit rapidity seen in “soft” proton-antiproton collisions at this energy. As can be seen in Fig. 4.9, the charged particle density in the “transverse” region is a function of  $P_{T(\text{jet}\#1)}$  and rises very rapidly at low  $P_{T(\text{jet}\#1)}$  values. The “transverse” charged multiplicity doubles in going from  $P_{T(\text{jet}\#1)} = 1.5$  GeV to  $P_{T(\text{jet}\#1)} = 2.5$  GeV and then forms an approximately constant “plateau” for  $P_{T(\text{jet}\#1)} > 6$  GeV.

### (1) “Transverse” $\langle N_{\text{chg}} \rangle$ and $\langle P_{T\text{sum}} \rangle$ versus $P_{T(\text{jet}\#1)}$

Fig. 5.1 and Fig. 5.2 compare the “transverse”  $\langle N_{\text{chg}} \rangle$  and the “transverse”  $\langle P_{T\text{sum}} \rangle$ , respectively, with the QCD “hard scattering” Monte-Carlo predictions of Herwig 5.9, Isajet 7.32, and Pythia 6.115. Fig. 5.3 and Fig. 5.4 compare the “transverse”  $\langle N_{\text{chg}} \rangle$  and the “transverse”  $\langle P_{T\text{sum}} \rangle$ , respectively, with three versions of Pythia (6.115, 6.125, and no multiple scattering, see Table 2). Pythia with no multiple parton scattering does not have enough activity in the underlying event. Pythia 6.115 fits the “transverse”  $\langle N_{\text{chg}} \rangle$  the best, but overshoots slightly the “toward”  $\langle N_{\text{chg}} \rangle$  in Fig. 4.12. Isajet has a lot of activity in the underlying event, but gives the wrong  $P_{T(\text{jet}\#1)}$  dependence. Instead of a “plateau”, Isajet predicts a rising “transverse”  $\langle N_{\text{chg}} \rangle$  and gives too much activity at large  $P_{T(\text{jet}\#1)}$  values. Herwig does not have enough “transverse”  $\langle P_{T\text{sum}} \rangle$ .

We expect the “transverse” region to be composed predominately from particles that arise from the break-up of the beam and target and from initial-state radiation. This is clearly the case as can be seen in Fig. 5.5 where the predictions of Isajet for the “transverse” region are divided into three categories: beam-beam remnants, initial-state radiation, and outgoing jets plus final-state radiation. It is interesting to see that it is the beam-beam remnants that are producing the

approximately constant “plateau”. The contributions from initial-state radiation and from the outgoing hard scattering jets both increase as  $P_{T(\text{jet}\#1)}$  increases. In fact, for Isajet it is the sharp rise in the initial-state radiation component that is causing the disagreement with the data for  $P_{T(\text{jet}\#1)} > 20$  GeV.

As we explained in Section II, for Herwig and Pythia it makes no sense to distinguish between particles that arise from initial-state radiation from those that arise from final-state radiation, but one can separate the “hard scattering component” from the beam-beam remnants. For Pythia the beam-beam remnants include contributions from multiple parton scattering as illustrated in Fig. 1.2. Fig. 5.6 and Fig. 5.7 compare the “transverse”  $\langle N_{\text{chg}} \rangle$  with the QCD “hard scattering” Monte-Carlo predictions of Herwig 5.9 and Pythia 6.115, respectively. Here the predictions are divided into two categories: charged particles that arise from the break-up of the beam and target (*beam-beam remnants*), and charged particles that result from the outgoing jets plus initial and final-state radiation (*hard scattering component*). As was the case with Isajet the beam-beam remnants form the approximately constant “plateau” and the hard scattering component increase as  $P_{T(\text{jet}\#1)}$  increases. However, the hard scattering component of Herwig and Pythia does not rise nearly as fast as the hard scattering component of Isajet. This can be seen clearly in Fig. 5.8 where we compare directly the hard scattering component (*outgoing jets plus initial and final-state radiation*) of the “transverse”  $\langle N_{\text{chg}} \rangle$  from Isajet 7.32, Herwig 5.9, and Pythia 6.115. Pythia and Herwig are similar and rise gently as  $P_{T(\text{jet}\#1)}$  increases, whereas Isajet produces a much sharper increase as  $P_{T(\text{jet}\#1)}$  increases.

There are two reasons why the hard scattering component of Isajet is different from Herwig and Pythia. The first is due to different fragmentation schemes. Isajet uses independent fragmentation, which produces too many soft hadrons when partons begin to overlap. The second difference arises from the way the QCD Monte-Carlo produce “parton showers”. Isajet uses a leading-log picture in which the partons within the shower are ordered according to their invariant mass. Kinematics requires that the invariant mass of daughter partons be less than the invariant mass of the parent. Herwig and Pythia modify the leading-log picture to include “color coherence effects” which leads to “angle ordering” within the parton shower. Angle ordering produces less high  $P_T$  radiation within a parton shower which is what is seen in Fig. 5.8.

Without further study, we do not know how much of the difference seen in Fig. 5.8 is due to the different fragmentation schemes and how much is due to the color coherence effects.

The beam-beam remnant contribution to the “transverse”  $\langle N_{\text{chg}} \rangle$  is different for each of the QCD Monte-Carlo models. This can be seen in Fig. 5.9 where we compare directly the beam-beam remnant component of the “transverse”  $\langle N_{\text{chg}} \rangle$  from Isajet 7.32, Herwig 5.9, Pythia 6.115, and Pythia with no multiple parton interactions. Since we are considering only charged particles with  $P_T > 0.5$  GeV, the height of the “plateaus” in Fig. 5.9 is related to the transverse momentum distribution of the beam-beam remnant contributions. A steeper  $P_T$  distribution means less particles with  $P_T > 0.5$  GeV. Pythia uses multiple parton scattering to enhance the underlying event and we have included these contributions in the beam-beam remnants. For Pythia the height of the “plateau” in Fig. 5.9 can be adjusted by adjusting the amount of multiple parton scattering. Herwig and Isajet do not include multiple parton scattering. For Herwig and Isajet

the height of the “plateau” can be adjusted by changing the  $P_T$  distribution of the beam-beam remnants.

We will now study the  $P_T$  distribution of the beam-beam remnants by examining the transverse momentum distribution of the charged particles produced in the “transverse” region.

## (2) “Transverse” $P_T$ Distribution

Fig. 5.10 shows the data on the transverse momentum distribution of charged particles ( $P_T > 0.5$  GeV and  $|\eta| < 1$ ) in the “transverse” region defined in Fig. 4.2. The  $P_T(\text{jet\#1}) > 2$  and 5 GeV points are Min-Bias data and the  $P_T(\text{jet\#1}) > 30$  GeV points are JET20 data. Each point corresponds to the charge particle density  $dN_{\text{chg}}/dP_T$  and the integral of the distribution gives the average number of charged particles in the “transverse” region,  $\langle N_{\text{chg}}(\text{transverse}) \rangle$ . Since these distributions fall off sharply as  $P_T$  increases, it is essentially only the first point at low  $P_T$  that determines  $\langle N_{\text{chg}}(\text{transverse}) \rangle$ . The approximately constant “plateau” seen in Fig. 5.1 is a result of the low  $P_T$  points in Fig. 5.10 not changing much as  $P_T(\text{jet\#1})$  changes. However, the high  $P_T$  points in Fig. 5.10 do increase considerably as  $P_T(\text{jet\#1})$  increases. This cannot be seen by simply examining the average number of “transverse” particles. Fig. 5.10 shows the growth of the hard scattering component in the “transverse” region (*i.e.* three or more “hard scattering” jets).

For low values of  $P_T(\text{jet\#1})$  the  $P_T$  distribution in the “transverse” region is dominated by the beam-beam remnant contribution with very little “hard scattering”. This can be seen in Fig. 5.11, Fig. 5.12, and Fig. 5.13, where we compare the predictions of Herwig 5.9, Isajet 7.32, and Pythia 6.115, respectively, with the data from Fig. 4.10 for  $P_T(\text{jet\#1}) > 2$  GeV. Here one can see clearly that the beam-beam remnant component of both Isajet and Herwig has the wrong  $P_T$  dependence. Isajet and Herwig both predict too steep of a  $P_T$  distribution. Pythia does a better job, but is still slightly too steep. It is, of course, understandable that the Monte-Carlo models might be slightly off on the parameterization of the beam-beam remnants. This component can not be calculated from perturbation theory and must be determined from data.

In Fig. 5.14, Fig. 5.15, and Fig. 5.16 we compare the predictions of Herwig 5.9, Isajet 7.32, and Pythia 6.115, respectively, with the data from Fig. 4.10 for  $P_T(\text{jet\#1}) > 30$  GeV. All the models do well at describing the high  $P_T$  tail of the distribution. Isajet produces too many charged particles at low  $P_T$ . This is a result of the wrong  $P_T$  dependence for the beam-beam remnant contribution and from an overabundance of soft particles produced in the “hard scattering”. Fig. 5.15 shows that the large rise in the “transverse” charged multiplicity from the “hard scattering” component of Isajet seen in Fig. 5.8 comes from “soft” particles. This is to be expected from a model that employs independent fragmentation such as Isajet. Independent fragmentation does not differ much from “color string” or “cluster” fragmentation for the hard particles, but independent fragmentation produces too many soft particles (*i.e.* it double counts soft particles).

## VI. Summary and Conclusions

For proton-antiproton collisions at 1.8 TeV min-bias does not necessarily imply “soft” physics. There is a lot of QCD “hard scattering” in the Min-Bias data. We have studied both “local” leading jet observables and “global” observables where to fit the data the QCD Monte-Carlo models have to correctly describe the entire event structure. Our summary and conclusions are as follows.

### *The Evolution of Charge Particle Jets*

Charged particle jets are “born” somewhere around  $P_{T(\text{jet})}$  of about 2 GeV with, on the average, about 2 charged particles and grow to, on the average, about 10 charged particles at 50 GeV. The QCD “hard scattering” models describe quite well (*although not perfectly*) “local” leading jet observables such as the multiplicity distribution of charged particles within the leading jet, the “size” of the leading jet, the radial flow of charged particles and transverse momentum around the leading jet direction, and the momentum distribution of charged particles within the leading jet. In fact, the QCD “hard” scattering Monte-Carlo models agree as well with 2 GeV charged particle jets as they do with 50 GeV charged particle jets! The charge particle jets in the Min-Bias data are simply the extrapolation (*down to small  $P_T$* ) of the high transverse momentum jets observed in the JET20 data. For a fixed  $P_{T(\text{hard})}$ , the QCD “hard” scattering cross section grows with increasing collider energy. As the center-of-mass energy of a proton-antiproton collision grows, “hard” scattering becomes a larger and larger fraction of the total inelastic cross section. At 1.8 TeV “hard scattering” makes up a sizable part of the “hard core” inelastic cross section and a lot of min-bias events have 2 GeV or 3 GeV jets.

### *The “Underlying Event”*

A hard scattering collider event consists of large transverse momentum outgoing hadrons that originate from the large transverse momentum partons (*outgoing jets*) and also hadrons that originate from the break-up of the proton and antiproton (*beam-beam remnants*). The “underlying event” is formed from the beam-beam remnants, initial-state radiation, and possibly from multiple parton interactions. Our data show that the charged particle multiplicity and scalar  $P_T$  sum in the “underlying event” grows very rapidly with the transverse momentum of the leading charged particle jet and then forms an approximately constant “plateau” for  $P_{T(\text{jet}\#1)} > 6$  GeV. The height of this “plateau” is at least twice that observed in “soft” collisions at the same corresponding energy.

None of the QCD Monte-Carlo models we examined correctly describe all the properties of the underlying event seen in the data. Herwig 5.9 and Pythia 6.125 do not have enough activity in the underlying event. Pythia 6.115 has about the right amount of activity in the underlying event, but as a result produces too much overall charged multiplicity. Isajet 7.32 has a lot of activity in the underlying event, but with the wrong dependence on  $P_{T(\text{jet}\#1)}$ . Because Isajet uses independent fragmentation and Herwig and Pythia do not, there are clear differences in the hard scattering component (*mostly initial-state radiation*) of the underlying event between Isajet and the other two Monte-Carlo models. Here the data strongly favor Herwig and Pythia over Isajet.

The beam-beam remnant component of both Isajet 7.32 and Herwig 5.9 has the wrong  $P_T$  dependence. Isajet and Herwig both predict too steep of a  $P_T$  distribution. Pythia does a better job, but is still slightly too steep. It is, of course, understandable that the Monte-Carlo models might be somewhat off on the parameterization of the beam-beam remnants. This component cannot be calculated from perturbation theory and must be determined from data. With what we have learned from the data presented here, the beam-beam remnant component of the QCD “hard scattering” Monte-Carlo models can be tuned to better describe the overall event in proton-antiproton collisions.

## References and Footnotes

1. G. Marchesini and B. R. Webber, Nucl. Phys. **B310**, 461 (1988); I. G. Knowles, Nucl. Phys. **B310**, 571 (1988); S. Catani, G. Marchesini, and B. R. Webber, Nucl. Phys. **B349**, 635 (19991).
2. F. Paige and S. Protopopescu, BNL Report, BNL38034, 1986 (unpublished), version 7.32.
3. T. Sjostrand, Phys. Lett. **157B**, 321 (1985); M. Bengtsson, T. Sjostrand, and M. van Zijl, Z. Phys. **C32**, 67 (1986); T. Sjostrand and M. van Zijl, Phys. Rev. **D36**, 2019 (1987).
4. F. Abe *et al.*, Nucl. Instrum. Methods, **A271**, 387 (1988).

## Figures

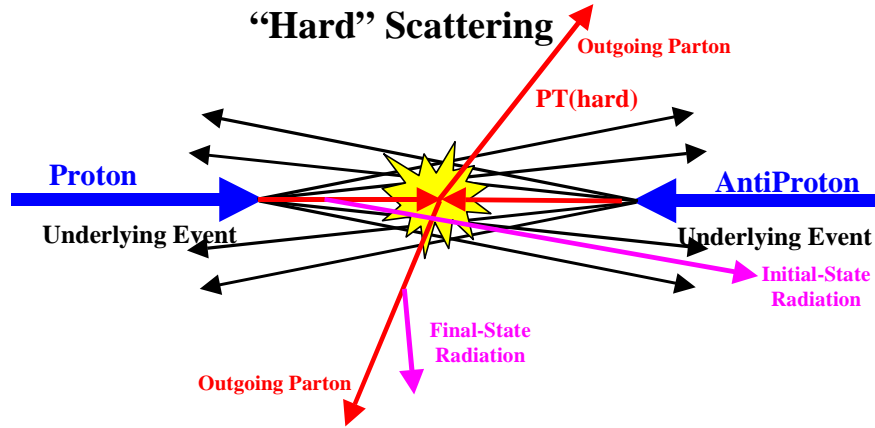


**Fig. 1.1.** Illustration of a proton-antiproton collision in which a “hard” 2-to-2 parton scattering with transverse momentum,  $P_T(\text{hard})$ , has occurred. The resulting event contains particles that originate from the two outgoing partons (plus final-state radiation) and particles that come from the breakup of the proton and antiproton (*i.e.* “beam-beam remnants”). The “underlying event” consists of the beam-beam remnants plus initial-state radiation.

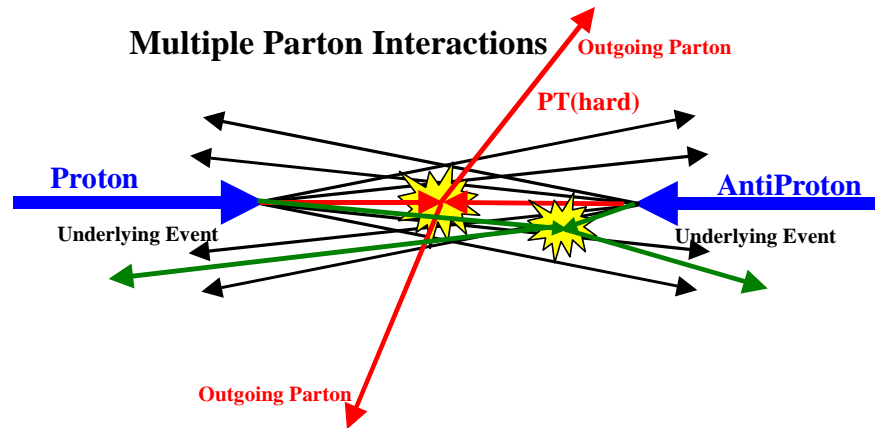


**Fig. 1.2.** Illustration of a proton-antiproton collision in which a multiple parton interaction has occurred. In addition to the “hard” 2-to-2 parton scattering with transverse momentum,  $P_T(\text{hard})$ , there is an additional “semi-hard” parton-parton scattering that contributes particles to the “underlying event”. For Pythia, we include the contributions from multiple parton scattering in the beam-beam remnant component.

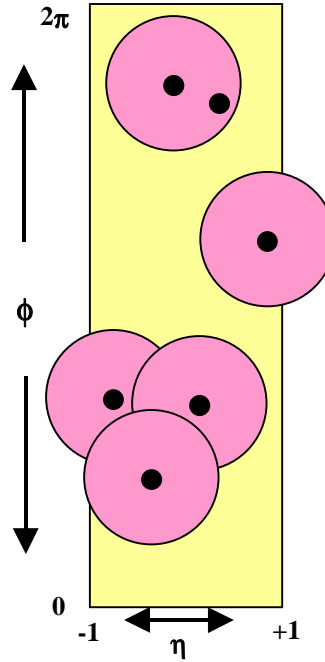


**Fig. 3.1.** Illustration of an event with six charged particles ( $P_T > 0.5$  GeV and  $|\eta| < 1$ ) and five charged “jets” (circular regions in  $\eta$ - $\phi$  space with  $R = 0.7$ ).

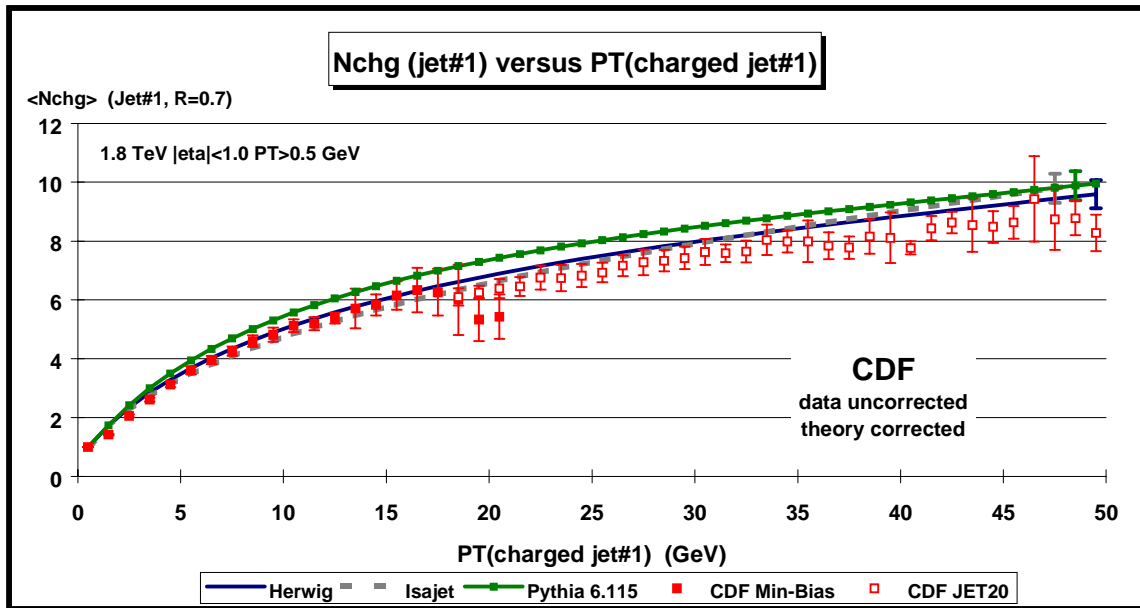


**Fig. 3.2.** Plot shows the average number of charged particles ( $P_T > 0.5$  GeV,  $|\eta| < 1$ ) within the leading charged jet ( $R = 0.7$ ) as a function of the  $P_T$  of the leading charged jet. The solid (open) points are Min-Bias (JET20) data. The errors on the (uncorrected) data include both statistical and correlated systematic uncertainties. The QCD “hard scattering” theory curves (Herwig 5.9, Isajet 7.32, Pythia 6.115) are corrected for the track finding efficiency and have an error (statistical plus systematic) of around 5%.

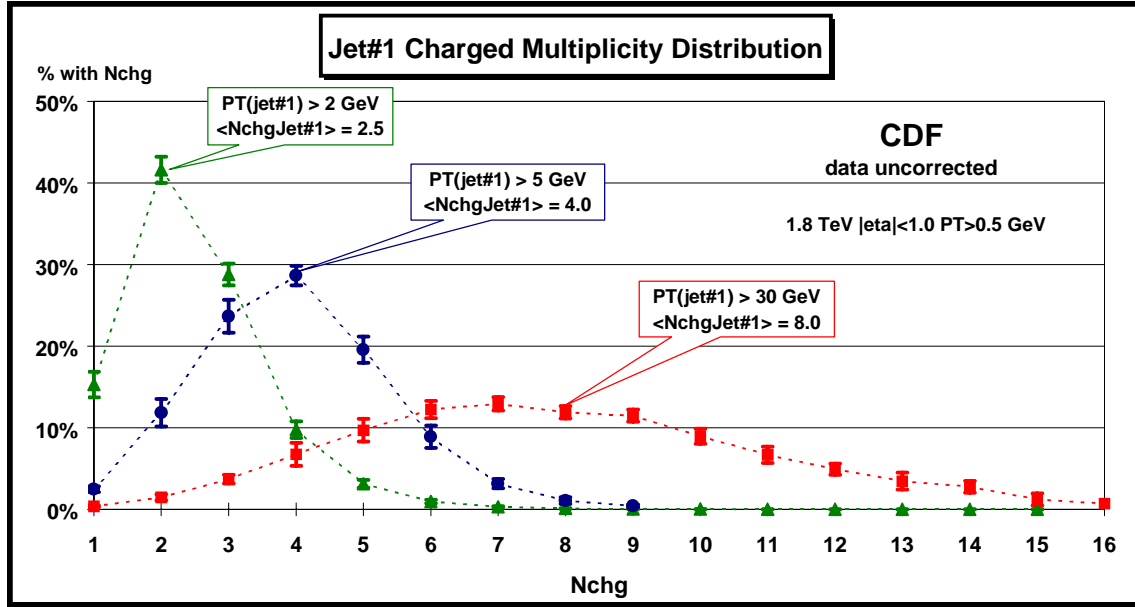


**Fig. 3.3.** Multiplicity distribution of charged particles ( $P_T > 0.5$  GeV and  $|\eta| < 1$ ) within jet#1 (*leading charged jet*) for  $P_T(\text{jet}\#1) > 2, 5$ , and  $30$  GeV. Plot shows the percentage of events in which the leading charged jet ( $R = 0.7$ ) contains  $N_{chg}$  charged particles. The  $P_T(\text{jet}\#1) > 2$  and  $5$  GeV points are Min-Bias data and the  $P_T(\text{jet}\#1) > 30$  GeV points are JET20 data. The dashed curves are to guide the eye. The errors on the (*uncorrected*) data include both statistical and correlated systematic uncertainties.

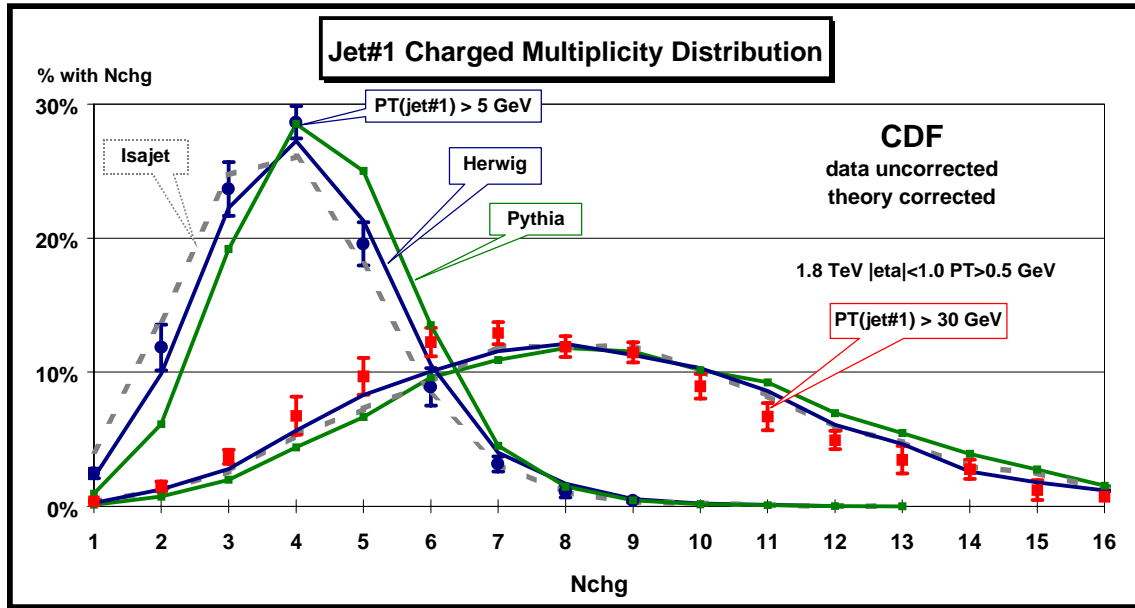


**Fig. 3.4.** Multiplicity distribution of charged particles ( $P_T > 0.5$  GeV and  $|\eta| < 1$ ) within jet#1 (*leading charged jet*) for  $P_T(\text{jet}\#1) > 5$  and  $30$  GeV from Fig. 3.3 compared with the QCD “hard scattering” Monte-Carlo predictions of Herwig 5.9, Isajet 7.32, and Pythia 6.115. Plot shows the percentage of events in which the leading charged jet ( $R = 0.7$ ) contains  $N_{chg}$  charged particles. The errors on the (*uncorrected*) data include both statistical and correlated systematic uncertainties. The QCD theory curves are corrected for the track finding efficiency and have an error (*statistical plus systematic*) of around 5%.

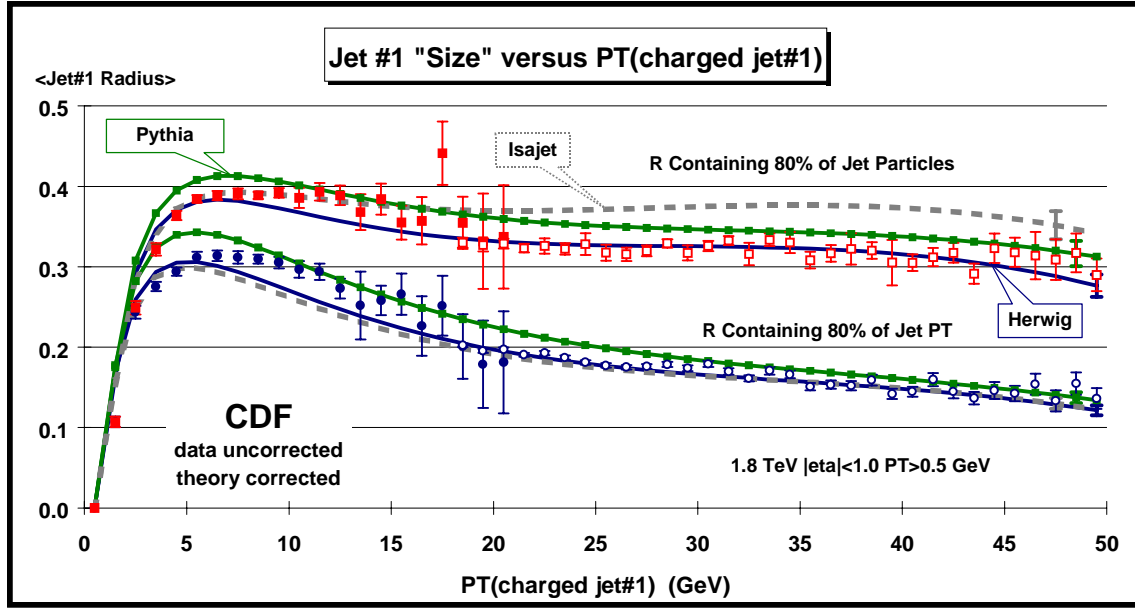


**Fig. 3.5.** Plot shows the average radius in  $\eta$ - $\phi$  space containing 80% of the charged particles (and 80% of the charged  $P_T$ ) as a function of the transverse momentum of the leading charged jet. The errors on the (*uncorrected*) data include both statistical and correlated systematic uncertainties. The QCD “hard scattering” theory curves (Herwig 5.9, Isajet 7.32, Pythia 6.115) are corrected for the track finding efficiency and have an error (*statistical plus systematic*) of around 5%.

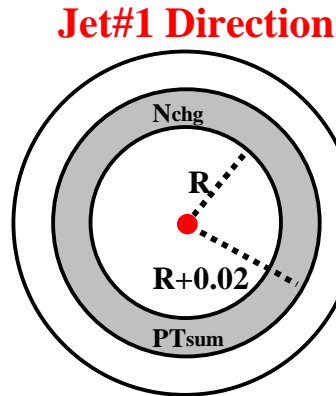


**Fig. 3.6.** Illustration of correlations in the radial distance  $R$  in  $\eta$ - $\phi$  space from the direction of the leading jet in the event, jet#1. The radius  $R$  is the distance in  $\eta$ - $\phi$  space between the leading jet and a charged particle with  $P_T > 0.5$  GeV and  $|\eta| < 1$ ,  $R^2 = (\Delta\eta)^2 + (\Delta\phi)^2$ . Plots of  $\langle N_{chg} \rangle$  and  $\langle P_{Tsum} \rangle$  as a function of  $R$  are referred to as “radial multiplicity flow” relative to jet#1 and “radial  $P_T$  flow” relative to jet#1, respectively.

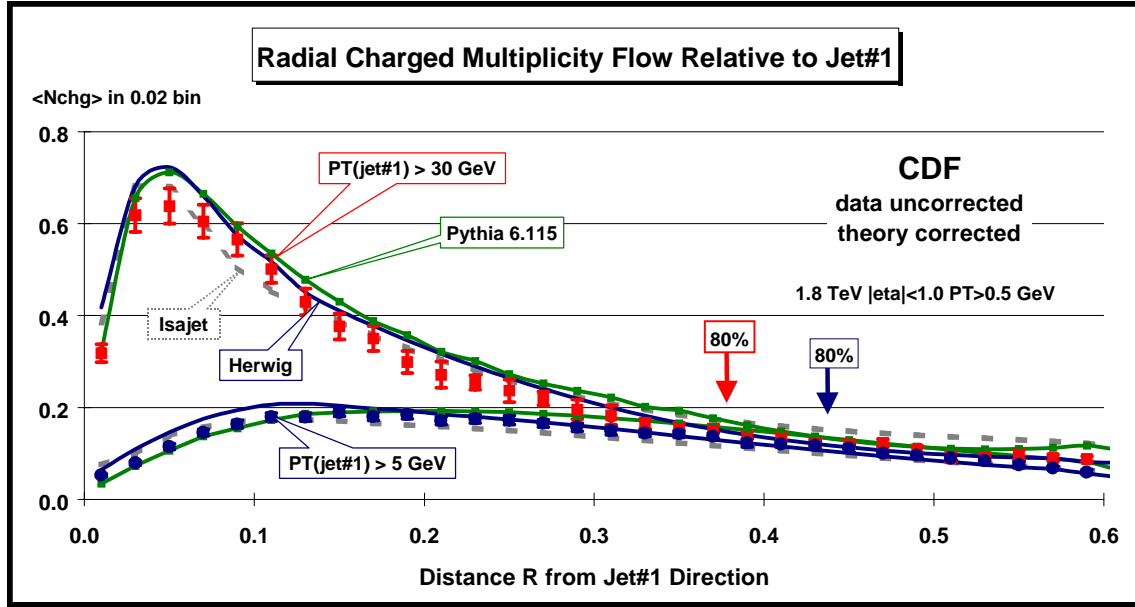


**Fig. 3.7.** Charged multiplicity flow in the radial distance  $R$  in  $\eta$ - $\phi$  space from jet#1 (*leading charged jet*) for charged particles with  $P_T > 0.5$  GeV and  $|\eta| < 1$  when  $P_T(\text{jet}\#1) > 5$  and 30 GeV. The points are  $\langle N_{\text{chg}} \rangle$  in a 0.02 bin of  $R$ . The  $P_T(\text{jet}\#1) > 5$  GeV points are Min-Bias data and the  $P_T(\text{jet}\#1) > 30$  GeV points are JET20 data. The data are compared with the QCD “hard scattering” Monte-Carlo predictions of Herwig 5.9, Isajet 7.32, and Pythia 6.115. The errors on the (*uncorrected*) data include both statistical and correlated systematic uncertainties. The theory curves are corrected for the track finding efficiency and have an error (*statistical plus systematic*) of around 5%. For an “average charged jet” with  $P_T(\text{jet}\#1) > 5$  GeV ( $> 30$  GeV), 80% of the charged particles lie within  $R = 0.44$  (0.38) as marked by the arrows.

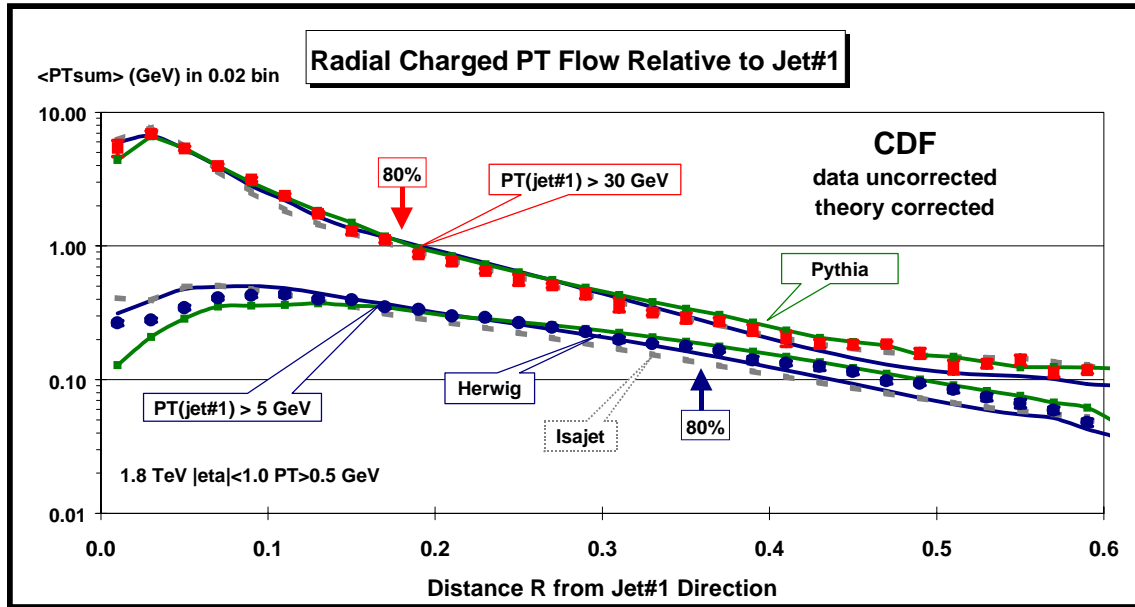


**Fig. 3.8.** Charged transverse momentum flow in the distance  $R$  in  $\eta$ - $\phi$  space from jet#1 (*leading charged jet*) for charged particles with  $P_T > 0.5$  GeV and  $|\eta| < 1$  when  $P_T(\text{jet}\#1) > 5$  and 30 GeV. The points are  $\langle P_{T\text{sum}} \rangle$  in a 0.02 bin of  $R$ . The  $P_T(\text{jet}\#1) > 5$  GeV points are Min-Bias data and the  $P_T(\text{jet}\#1) > 30$  GeV points are JET20 data. The data are compared with the QCD “hard scattering” Monte-Carlo predictions of Herwig 5.9, Isajet 7.32, and Pythia 6.115. The errors on the (*uncorrected*) data include both statistical and correlated systematic uncertainties. The theory curves are corrected for the track finding efficiency and have an error (*statistical plus systematic*) of around 5%. For an “average charged jet” with  $P_T(\text{jet}\#1) > 5$  GeV ( $> 30$  GeV), 80% of the jet  $P_T$  lies within  $R = 0.36$  (0.18) as marked by the arrows. (Note the *logarithmic scale* on the vertical axis.)

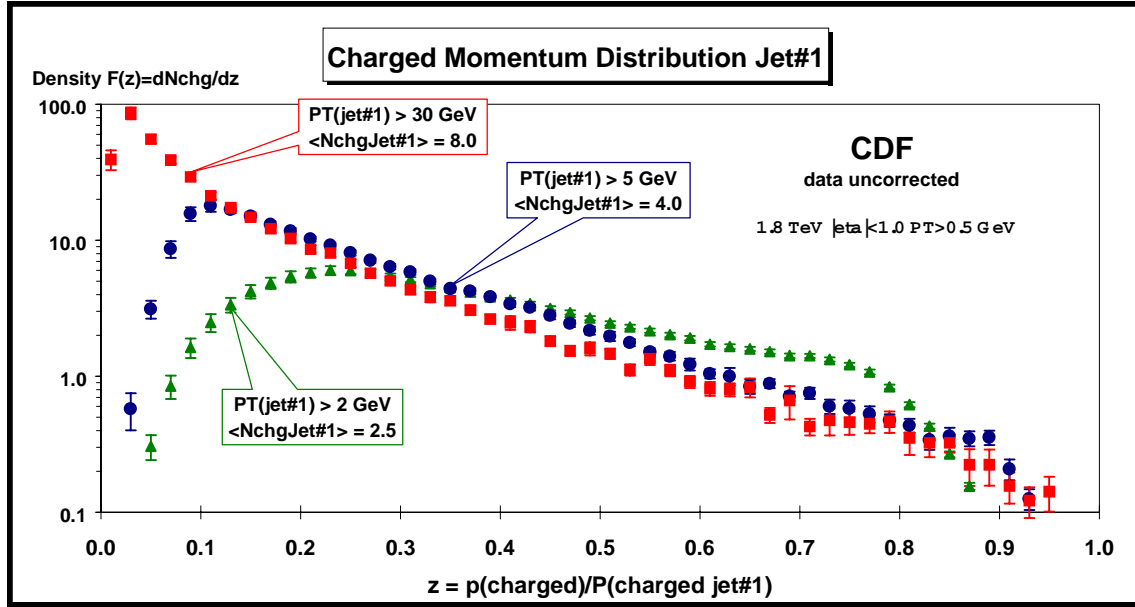


**Fig. 3.9.** Momentum distribution of charged particles ( $P_T > 0.5$  GeV and  $|\eta| < 1$ ) within jet#1 (*leading charged jet*). The points are the charged number density,  $F(z) = dN_{chg}/dz$ , where  $z = p/P(\text{charged jet\#1})$  is the ratio of the charged particle momentum to the charged momentum of jet#1. The integral of  $F(z)$  is the average number of particles within jet#1 (see Fig. 3.3). The  $P_T(\text{jet\#1}) > 2$  and  $5$  GeV points are Min-Bias data and the  $P_T(\text{jet\#1}) > 30$  GeV points are JET20 data. The errors on the (*uncorrected*) data include both statistical and correlated systematic uncertainties. (Note the *logarithmic scale* on the vertical axis.)

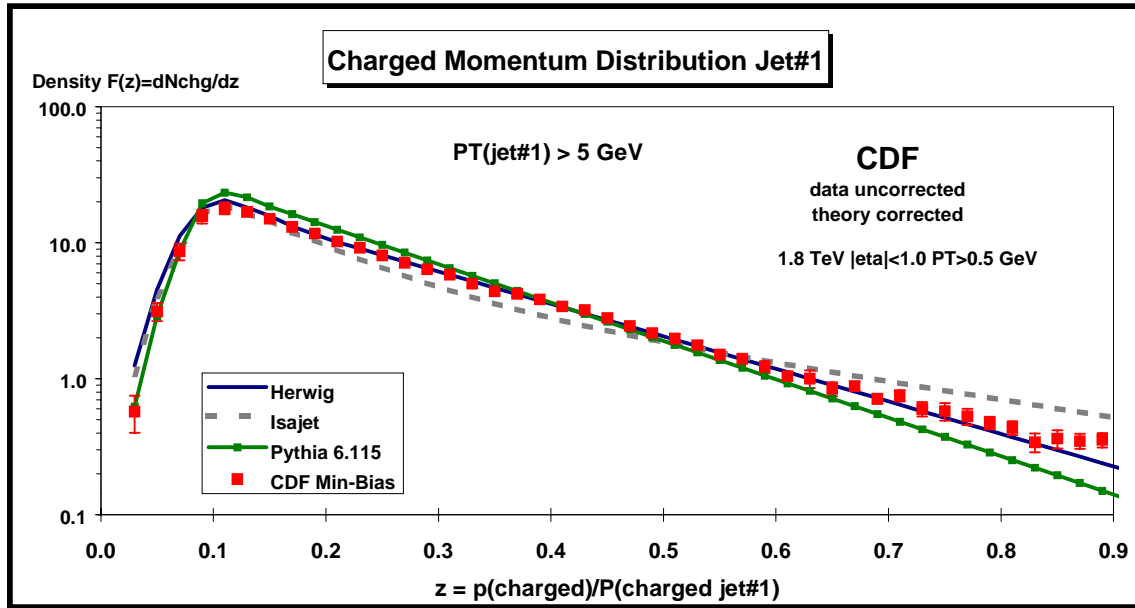


**Fig. 3.10.** Data from Fig. 3.9 on the momentum distribution of charged particles ( $P_T > 0.5$  GeV and  $|\eta| < 1$ ) within jet#1 (*leading charged jet*) for  $P_T(\text{jet\#1}) > 5$  GeV compared with the QCD “hard scattering” Monte-Carlo predictions of Herwig 5.9, Isajet 7.32, and Pythia 6.115. The points are the charged number density,  $F(z) = dN_{chg}/dz$ , where  $z = p/P(\text{charged jet\#1})$  is the ratio of the charged particle momentum to the charged momentum of jet#1. The errors on the (*uncorrected*) data include both statistical and correlated systematic uncertainties. The theory curves are corrected for the track finding efficiency and have an error (*statistical plus systematic*) of around 5%. (Note the *logarithmic scale* on the vertical axis.)

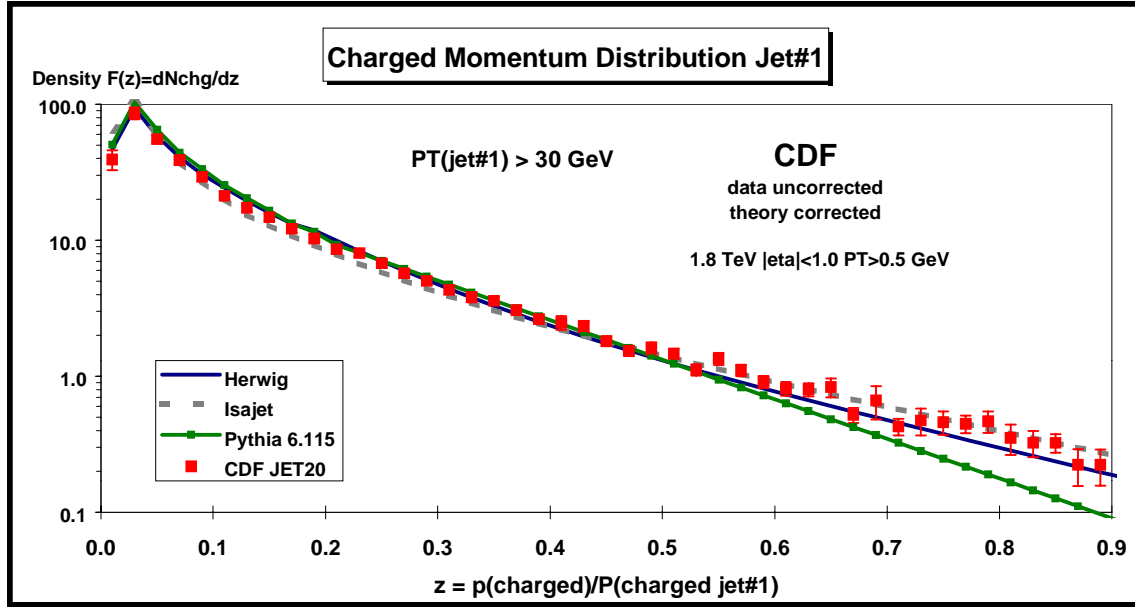


**Fig. 3.11.** Data from Fig. 3.9 on the momentum distribution of charged particles ( $P_T > 0.5$  GeV and  $|\eta| < 1$ ) within jet#1 (*leading charged jet*) for  $P_T(\text{jet}\#1) > 30$  GeV compared with the QCD “hard scattering” Monte-Carlo predictions of Herwig 5.9, Isajet 7.32, and Pythia 6.115. The points are the charged number density,  $F(z) = dN_{\text{chg}}/dz$ , where  $z = p/P(\text{charged jet}\#1)$  is the ratio of the charged particle momentum to the charged momentum of jet#1. The errors on the (*uncorrected*) data include both statistical and correlated systematic uncertainties. The theory curves are corrected for the track finding efficiency and have an error (*statistical plus systematic*) of around 5%. (Note the *logarithmic scale* on the vertical axis.)

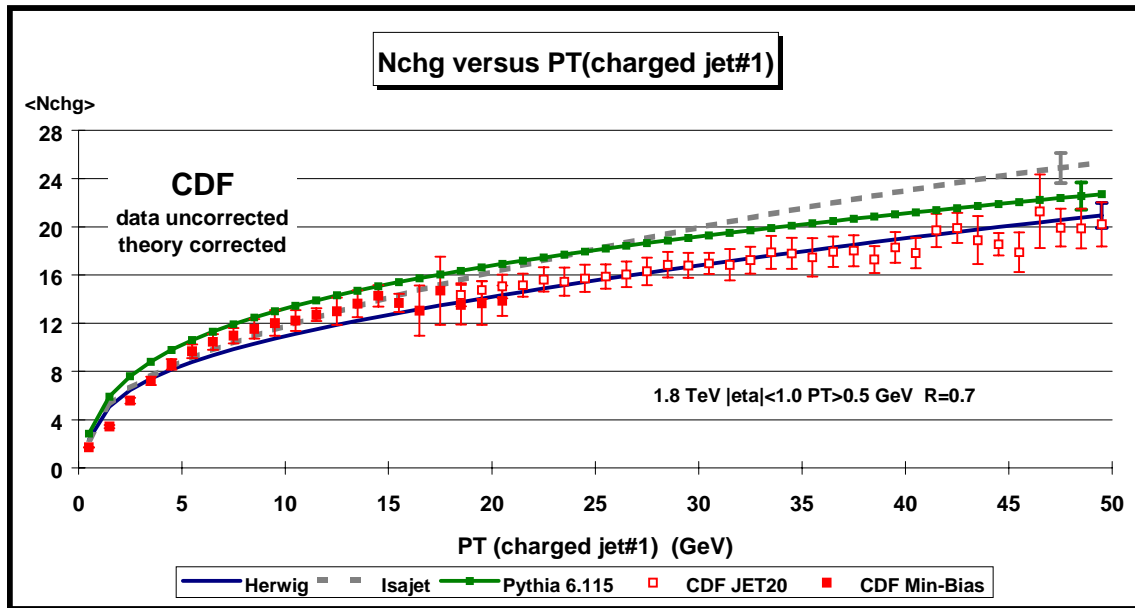


**Fig. 4.1.** Plot shows the average total number charged particles in the event ( $P_T > 0.5$  GeV,  $|\eta| < 1$  including jet#1) as a function of the transverse momentum of the leading charged jet. The solid (open) points are the Min-Bias (JET20) data. The errors on the (*uncorrected*) data include both statistical and correlated systematic uncertainties. The QCD “hard scattering” theory curves (Herwig 5.9, Isajet 7.32, Pythia 6.115) are corrected for the track finding efficiency and have an error (*statistical plus systematic*) of around 5%.

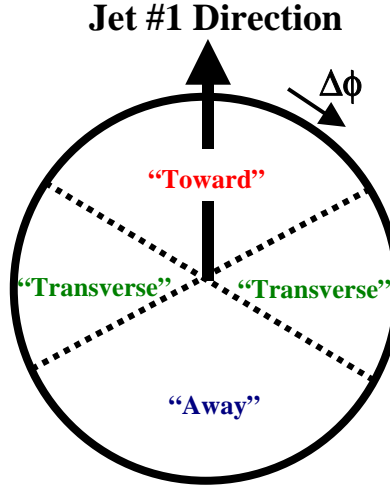


**Fig. 4.2.** Illustration of correlations in azimuthal angle  $\Delta\phi$  relative to the direction of the leading charged jet in the event, jet#1. The angle  $\Delta\phi = |\phi - \phi_{\text{jet}\#1}|$  is the relative azimuthal angle between charged particles and the direction of jet#1. The region  $|\Delta\phi| < 60^\circ$  is referred to as “toward” jet#1 (includes particles in jet#1) and the region  $|\Delta\phi| > 120^\circ$  is called “away” from jet#1. The “transverse” to jet#1 region is defined by  $60^\circ < |\Delta\phi| < 120^\circ$ . Each region, “toward”, “transverse”, and “away” covers the same range  $|\Delta\eta| \times |\Delta\phi| = 2 \times 120^\circ$ . Plots of  $\langle N_{\text{chg}} \rangle$  and  $\langle P_{\text{Tsum}} \rangle$  as a function of  $\Delta\phi$  are referred to as “multiplicity flow in  $\phi$ ” relative to jet#1 and “transverse momentum flow in  $\phi$ ” relative to jet#1, respectively.

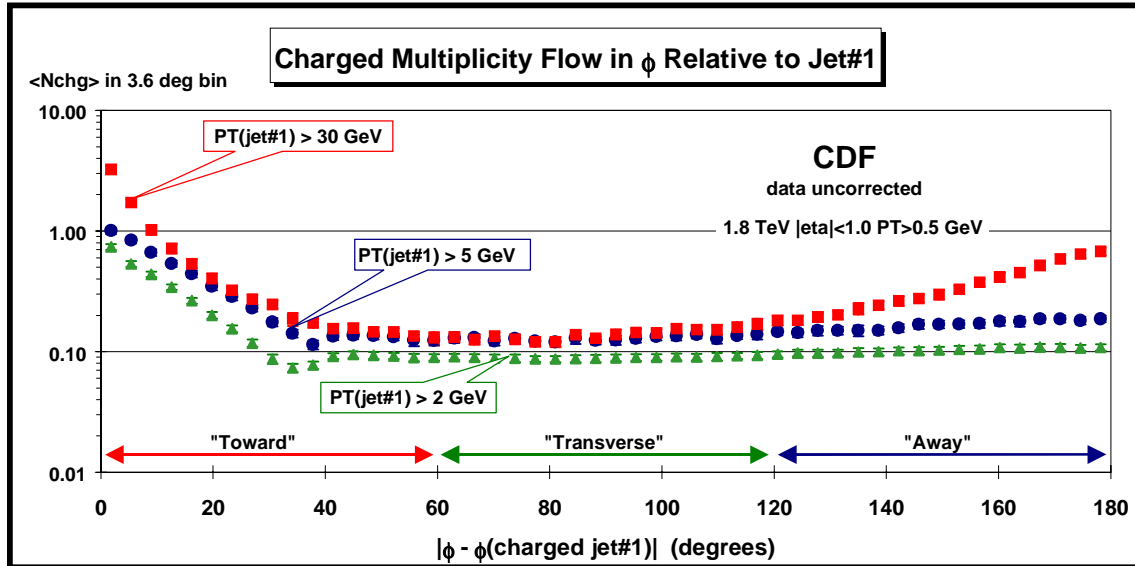


**Fig. 4.3.** Average number of charged particles ( $P_{\text{T}} > 0.5$  GeV,  $|\eta| < 1$ ) as a function of the relative azimuthal angle,  $|\Delta\phi|$ , between the particle and jet#1 (leading charged jet) for  $P_{\text{T}}(\text{jet}\#1) > 2, 5$ , and  $30$  GeV. Each point corresponds to the  $\langle N_{\text{chg}} \rangle$  in a  $3.6^\circ$  bin. The  $P_{\text{T}}(\text{jet}\#1) > 2$  and  $5$  GeV points are the Min-Bias data and the  $P_{\text{T}}(\text{jet}\#1) > 30$  GeV points are JET20 data. The errors on the (uncorrected) data include both statistical and correlated systematic uncertainties. The “toward”, “transverse”, and “away” regions are defined in Fig. 4.2. (Note the logarithmic scale on the vertical axis.)

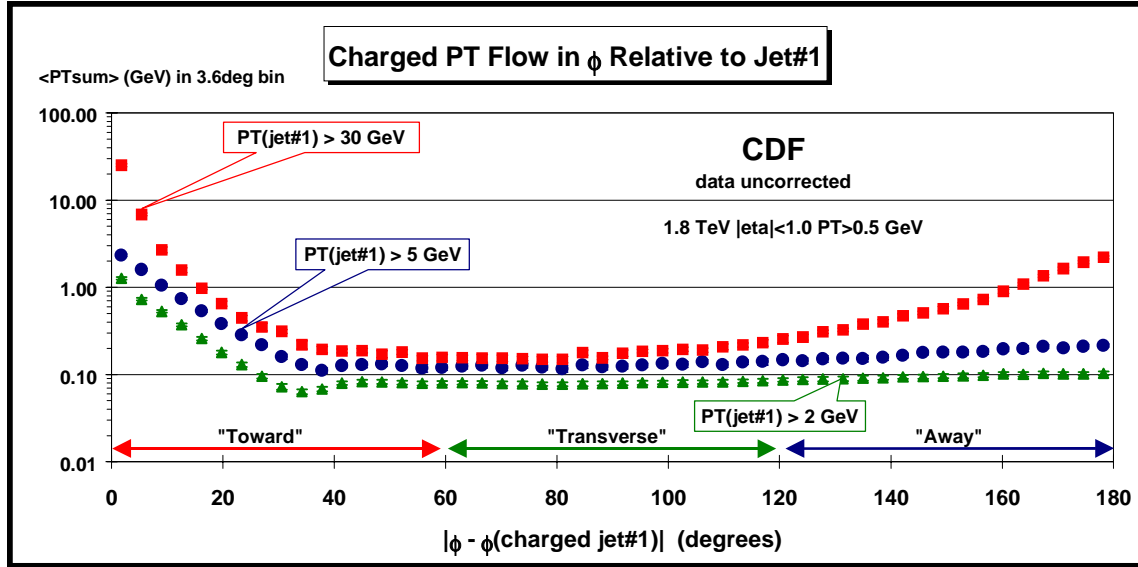


**Fig. 4.4.** Average *scalar*  $P_T$  sum of charged particles ( $P_T > 0.5$  GeV,  $|\eta| < 1$ ) as a function of the relative azimuthal angle,  $|\Delta\phi|$ , between the particle and jet#1 (*leading charged jet*) for  $P_T(\text{jet}\#1) > 2, 5$ , and  $30$  GeV. Each point corresponds to the  $\langle P_T \text{sum} \rangle$  in a  $3.6^\circ$  bin. The  $P_T(\text{jet}\#1) > 2$  and  $5$  GeV points are the Min-Bias data and the  $P_T(\text{jet}\#1) > 30$  GeV points are JET20 data. The errors on the (*uncorrected*) data include both statistical and correlated systematic uncertainties. The “toward”, “transverse”, and “away” regions are defined in Fig. 4.2. (Note the *logarithmic scale* on the vertical axis.)

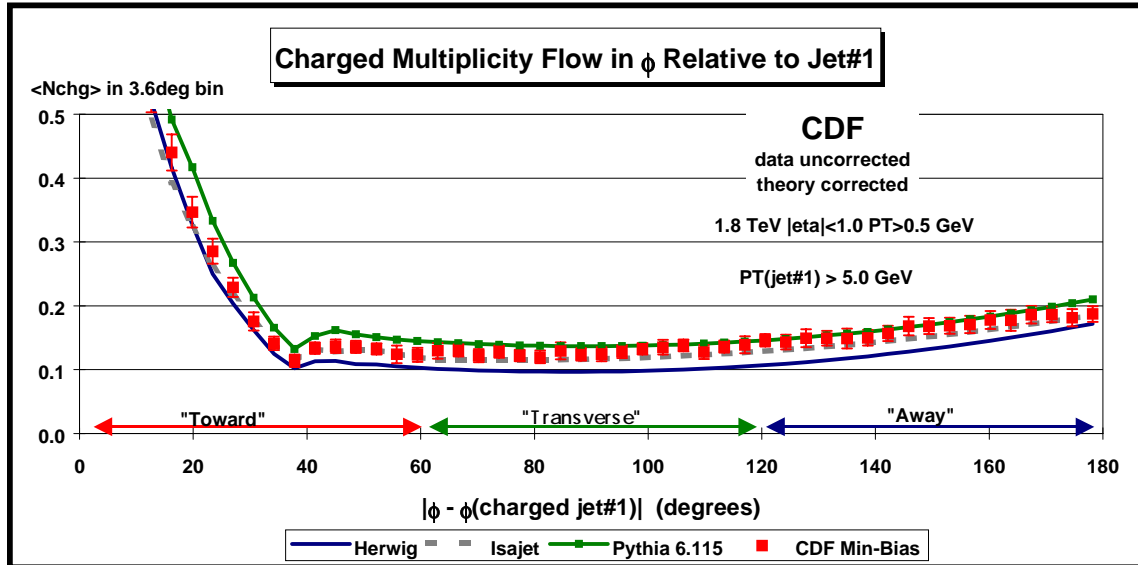


**Fig. 4.5.** Data from Fig. 4.3 on the average number of charged particles ( $P_T > 0.5$  GeV,  $|\eta| < 1$ ) as a function of the relative azimuthal angle,  $|\Delta\phi|$ , between the particle and jet#1 (*leading charged jet*) for  $P_T(\text{jet}\#1) > 5$  GeV compared to QCD “hard scattering” Monte-Carlo predictions of Herwig 5.9, Isajet 7.32, and Pythia 6.115. Each point corresponds to the  $\langle N_{\text{chg}} \rangle$  in a  $3.6^\circ$  bin. The errors on the (*uncorrected*) data include both statistical and correlated systematic uncertainties. The theory curves are corrected for the track finding efficiency and have an error (*statistical plus systematic*) of around 5%.

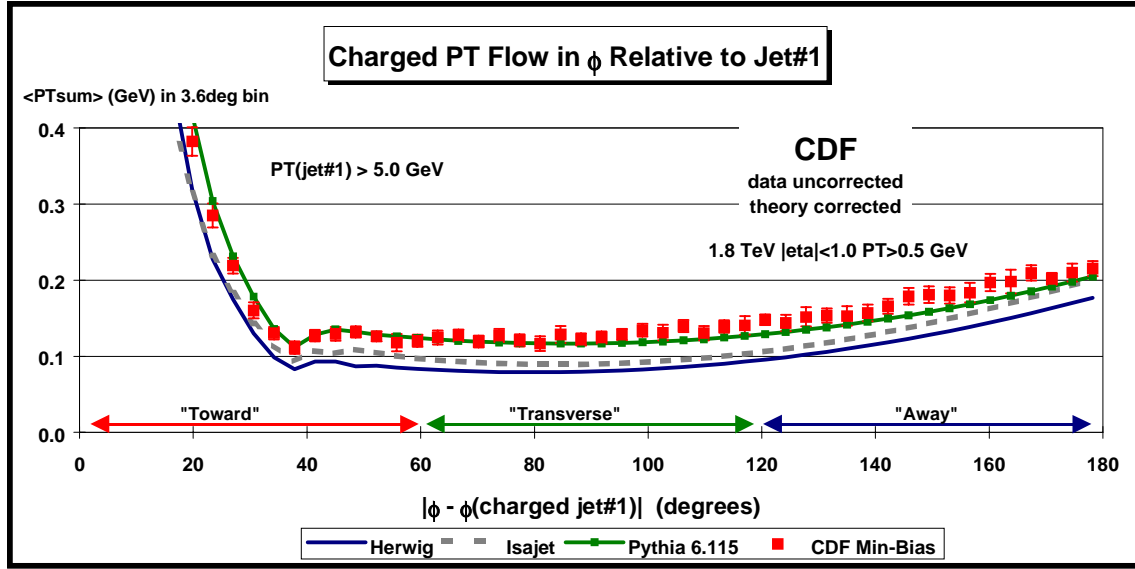


**Fig. 4.6.** Data from Fig. 4.4 on the average *scalar*  $P_T$  sum of charged particles as a function of the relative azimuthal angle,  $|\Delta\phi|$ , between the particle and jet#1 (*leading charged jet*) for  $P_{T(jet\#1)} > 5$  GeV compared to the QCD “hard scattering” Monte-Carlo predictions of Herwig 5.9, Isajet 7.32, and Pythia 6.115. Each point corresponds to the  $\langle PT_{sum} \rangle$  in a  $3.6^\circ$  bin. The errors on the (*uncorrected*) data include both statistical and correlated systematic uncertainties. The theory curves are corrected for the track finding efficiency and have an error (*statistical plus systematic*) of around 5%.

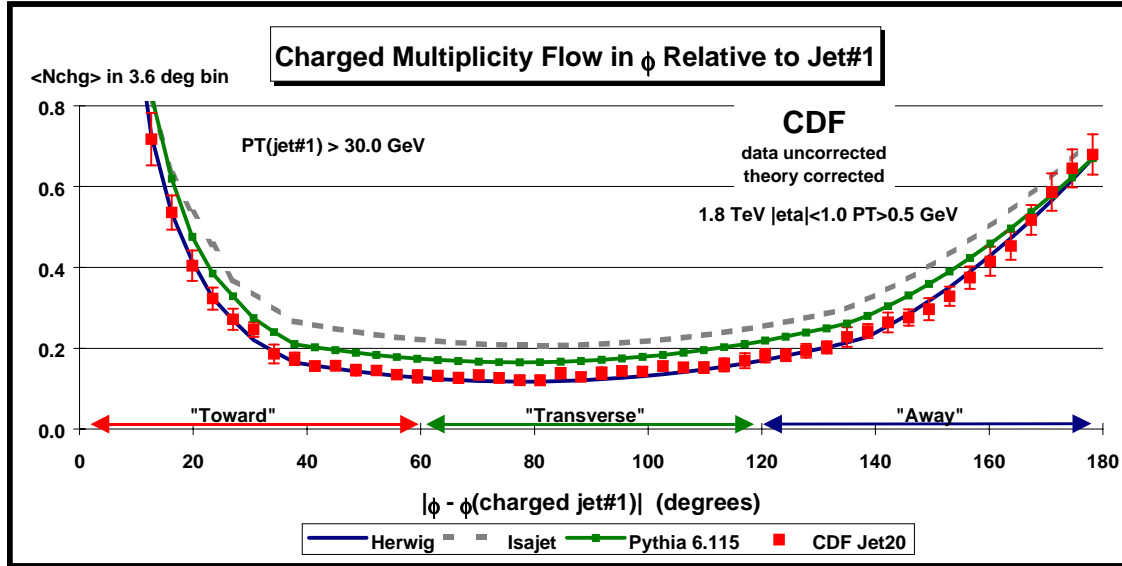


**Fig. 4.7.** Data from Fig. 4.3 on the average number of charged particles ( $P_T > 0.5$  GeV,  $|\eta| < 1$ ) as a function of the relative azimuthal angle,  $|\Delta\phi|$ , between the particle and jet#1 (*leading charged jet*) for  $P_{T(jet\#1)} > 30$  GeV compared to QCD “hard scattering” Monte-Carlo predictions of Herwig 5.9, Isajet 7.32, and Pythia 6.115. Each point corresponds to the  $\langle N_{chg} \rangle$  in a  $3.6^\circ$  bin. The errors on the (*uncorrected*) data include both statistical and correlated systematic uncertainties. The theory curves are corrected for the track finding efficiency and have an error (*statistical plus systematic*) of around 5%.

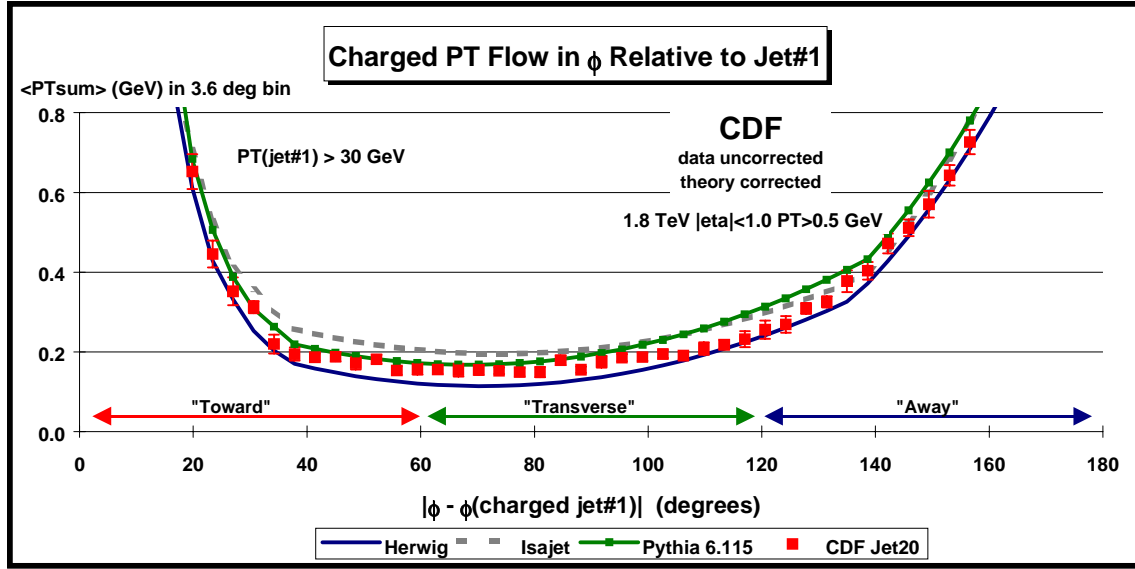


**Fig. 4.8.** Data from Fig. 4.4 on the average *scalar*  $P_T$  sum of charged particles as a function of the relative azimuthal angle,  $|\Delta\phi|$ , between the particle and jet#1 (*leading charged jet*) for  $P_{T}(\text{jet}\#1) > 30$  GeV compared to the QCD “hard scattering” Monte-Carlo predictions of Herwig 5.9, Isajet 7.32, and Pythia 6.115. Each point corresponds to the  $\langle P_{T\text{sum}} \rangle$  in a  $3.6^\circ$  bin. The errors on the (*uncorrected*) data include both statistical and correlated systematic uncertainties. The theory curves are corrected for the track finding efficiency and have an error (*statistical plus systematic*) of around 5%.

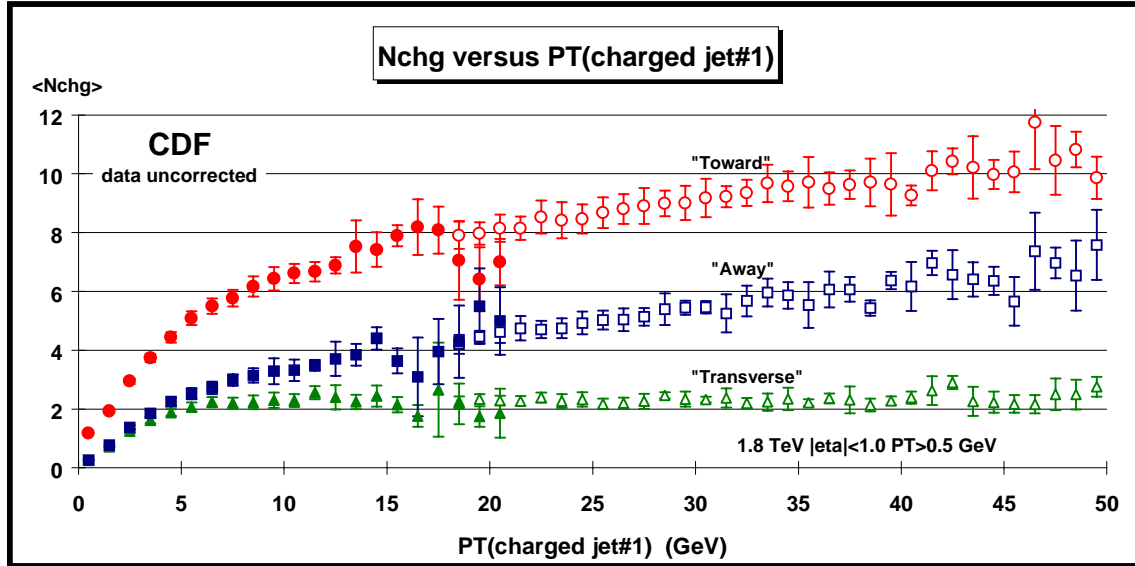


**Fig. 4.9.** The average number of “toward” ( $|\Delta\phi| < 60^\circ$ ), “transverse” ( $60 < |\Delta\phi| < 120^\circ$ ), and “away” ( $|\Delta\phi| > 120^\circ$ ) charged particles ( $P_T > 0.5$  GeV,  $|\eta| < 1$  including jet#1) as a function of the transverse momentum of the leading charged jet. Each point corresponds to the  $\langle N_{\text{chg}} \rangle$  in a 1 GeV bin. The solid (open) points are the Min-Bias (JET20) data. The errors on the (*uncorrected*) data include both statistical and correlated systematic uncertainties. The “toward”, “transverse”, and “away” regions are defined in Fig. 4.2 and shown on Fig. 4.3.

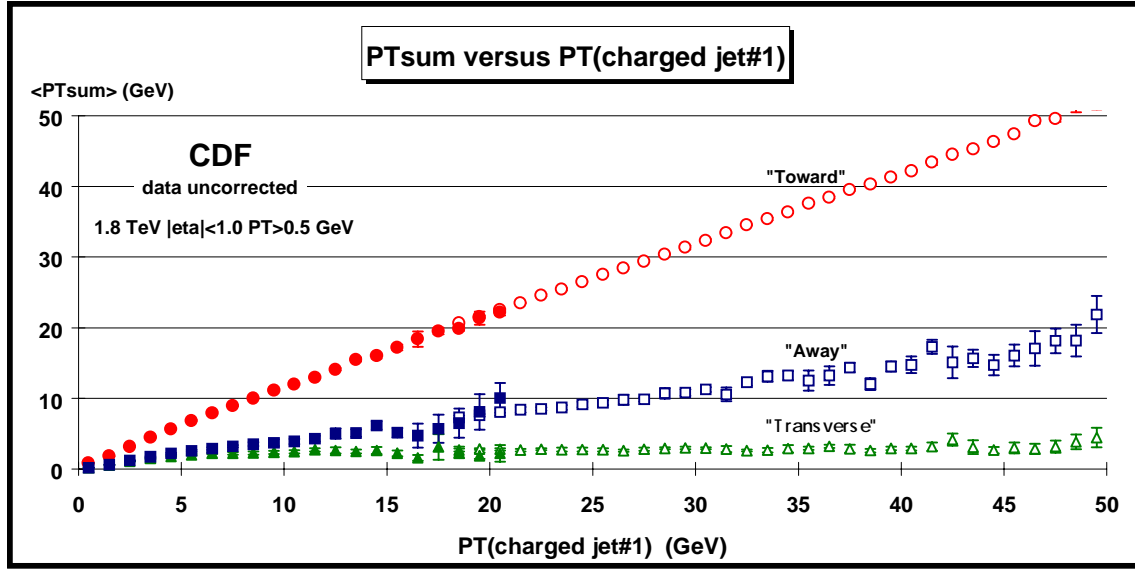


**Fig. 4.10.** The average *scalar*  $P_T$  sum of “toward” ( $|\Delta\phi| < 60^\circ$ ), “transverse” ( $60 < |\Delta\phi| < 120^\circ$ ), and “away” ( $|\Delta\phi| > 120^\circ$ ) charged particles ( $P_T > 0.5$  GeV,  $|\eta| < 1$  including jet#1) as a function of the transverse momentum of the leading charged jet. Each point corresponds to the  $\langle P_T \text{sum} \rangle$  in a 1 GeV bin. The solid (open) points are the Min-Bias (JET20) data. The errors on the (*uncorrected*) data include both statistical and correlated systematic uncertainties. The “toward”, “transverse”, and “away” regions are defined in Fig. 4.2 and shown on Figs. 4.4.

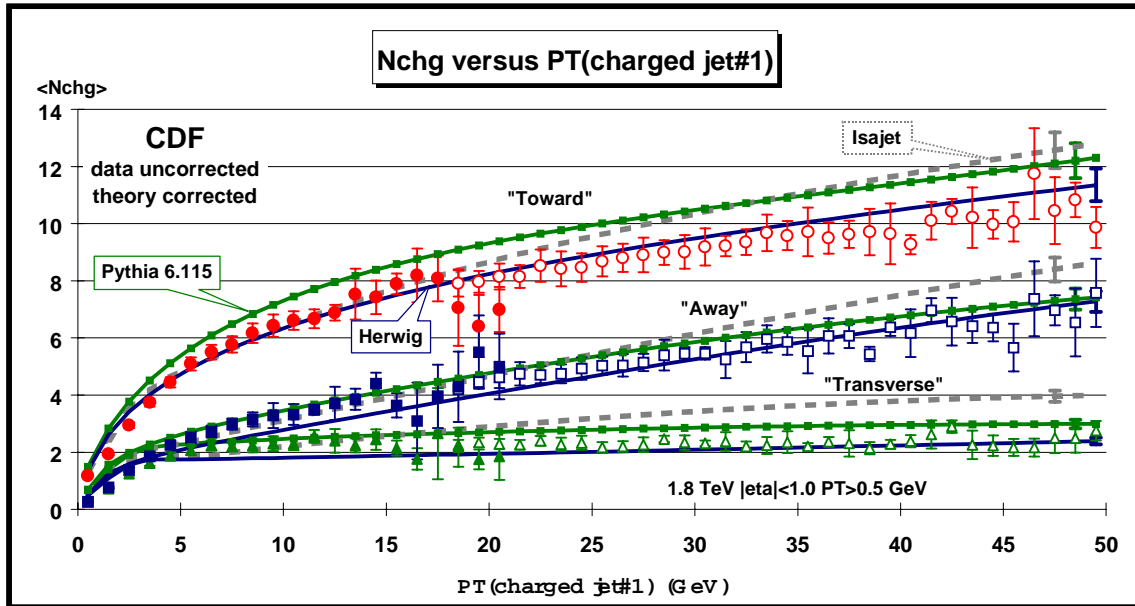


**Fig. 4.11.** Data from Fig. 4.9 on the average number of “toward” ( $|\Delta\phi| < 60^\circ$ ), “transverse” ( $60 < |\Delta\phi| < 120^\circ$ ), and “away” ( $|\Delta\phi| > 120^\circ$ ) charged particles ( $P_T > 0.5$  GeV,  $|\eta| < 1$  including jet#1) as a function of the transverse momentum of the leading charged jet compared to QCD “hard scattering” Monte-Carlo predictions of Herwig 5.9, Isajet 7.32, and Pythia 6.115. The errors on the (*uncorrected*) data include both statistical and correlated systematic uncertainties. The theory curves are corrected for the track finding efficiency and have an error (*statistical plus systematic*) of around 5%.

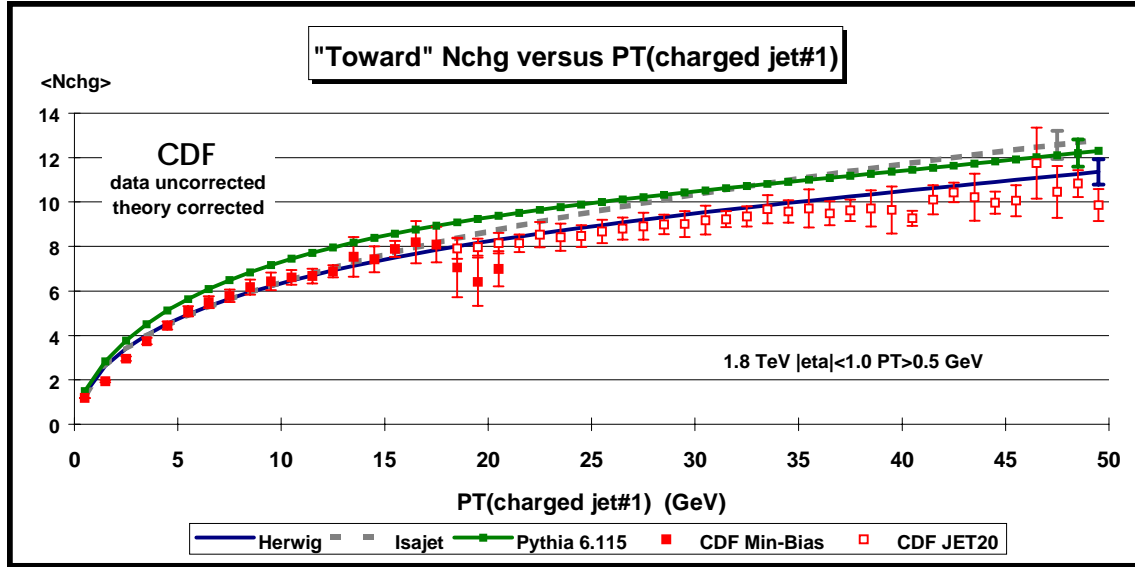


**Fig. 4.12.** Data from Fig.4.9 on the average number of charged particles ( $P_T > 0.5$  GeV and  $|\eta| < 1$ ) as a function of  $P_T$  (jet#1) (*leading charged jet*) for the “toward” region defined in Fig. 4.2 compared with the QCD “hard scattering” Monte-Carlo predictions of Herwig 5.9, Isajet 7.32, and Pythia 6.115. Each point corresponds to the “toward”  $\langle N_{chg} \rangle$  in a 1 GeV bin. The errors on the (*uncorrected*) data include both statistical and correlated systematic uncertainties. The theory curves are corrected for the track finding efficiency and have an error (*statistical plus systematic*) of around 5%.

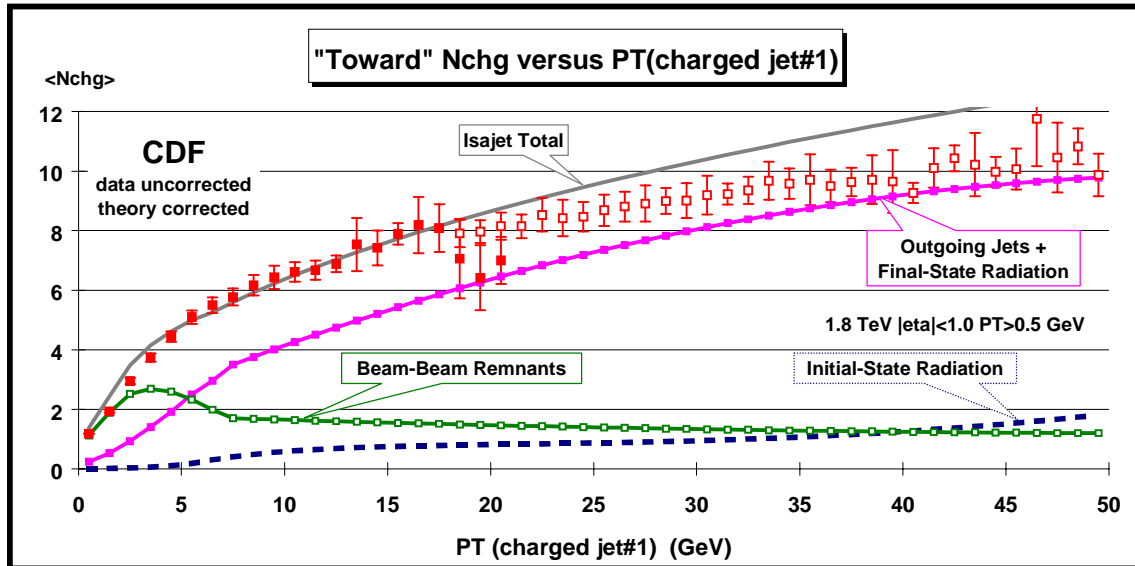


**Fig. 4.13.** Data from Fig. 4.9 on the average number of charged particles ( $P_T > 0.5$  GeV and  $|\eta| < 1$ ) as a function of  $P_T$  (jet#1) (*leading charged jet*) for the “toward” region defined in Fig. 4.2 compared with the QCD “hard scattering” Monte-Carlo predictions of Isajet 7.32. The predictions of Isajet are divided into three categories: charged particles that arise from the break-up of the beam and target (*beam-beam remnants*), charged particles that arise from initial-state radiation, and charged particles that result from the outgoing jets plus final-state radiation (see Fig. 1.1). The errors on the (*uncorrected*) data include both statistical and correlated systematic uncertainties. The theory curves are corrected for the track finding efficiency and have an error (*statistical plus systematic*) of around 5%.

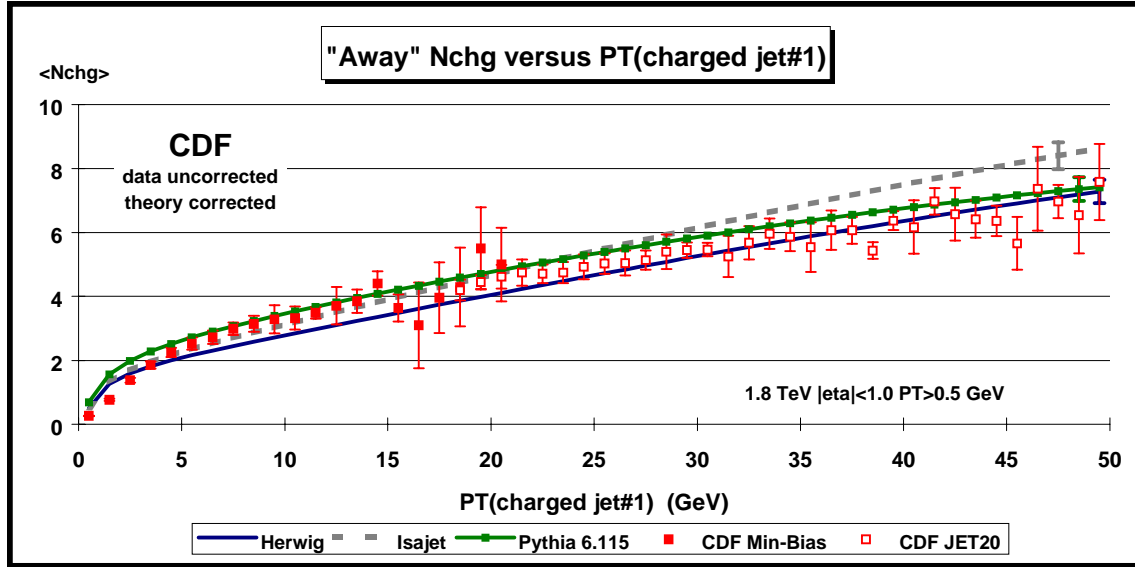


**Fig. 4.14.** Data from Fig.4.9 on the average number of charged particles ( $P_T > 0.5$  GeV and  $|\eta| < 1$ ) as a function of  $P_T(\text{jet}\#1)$  (leading charged jet) for the “away” region defined in Fig. 4.2 compared with the QCD “hard scattering” Monte-Carlo predictions of Herwig 5.9, Isajet 7.32, and Pythia 6.115. The errors on the (*uncorrected*) data include both statistical and correlated systematic uncertainties. The theory curves are corrected for the track finding efficiency and have an error (*statistical plus systematic*) of around 5%.

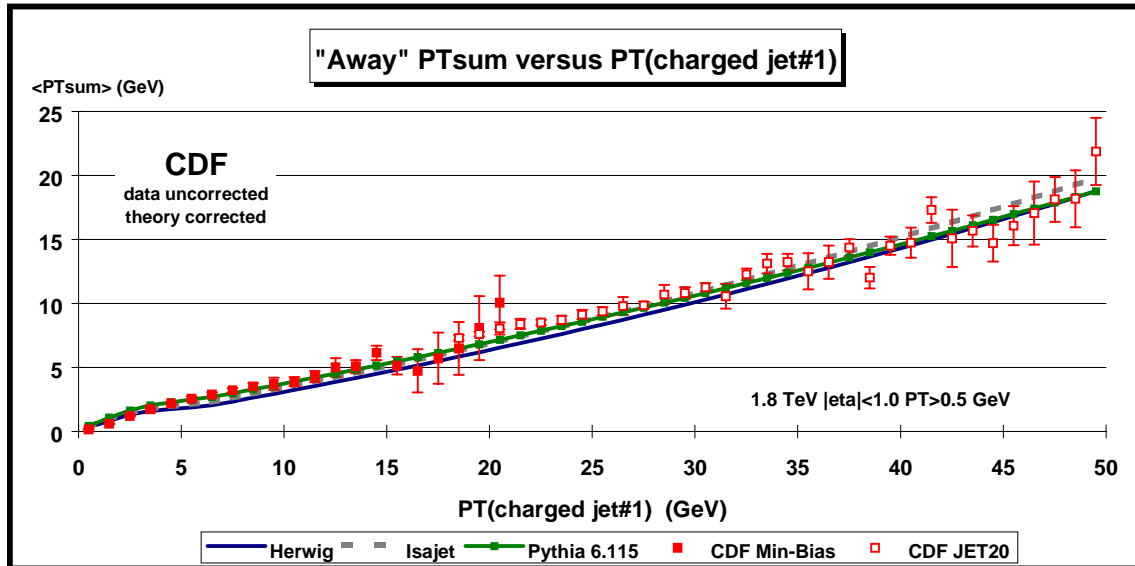


**Fig. 4.15.** Data from Fig. 4.10 on the average scalar  $P_T$  sum of charged particles ( $P_T > 0.5$  GeV and  $|\eta| < 1$ ) as a function of  $P_T(\text{jet}\#1)$  (leading charged jet) for the “away” region defined in Fig. 4.2 compared with the QCD “hard scattering” Monte-Carlo predictions of Herwig 5.9, Isajet 7.32, and Pythia 6.115. The errors on the (*uncorrected*) data include both statistical and correlated systematic uncertainties. The theory curves are corrected for the track finding efficiency and have an error (*statistical plus systematic*) of around 5%.

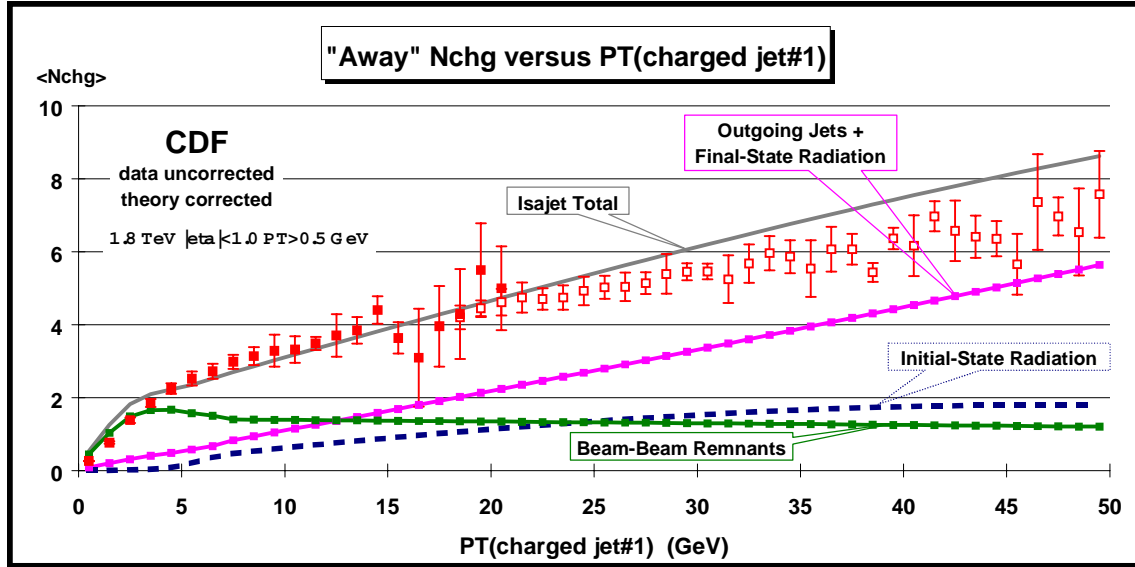


**Fig. 4.16.** Data from Fig.4.9 on the average number of charged particles ( $P_T > 0.5$  GeV and  $|\eta| < 1$ ) as a function of  $P_T(\text{jet\#1})$  (leading charged jet) for the “away” region defined in Fig. 4.2 compared with the QCD “hard scattering” Monte-Carlo predictions of Isajet 7.32. The predictions of Isajet are divided into three categories: charged particles that arise from the break-up of the beam and target (*beam-beam remnants*), charged particles that arise from initial-state radiation, and charged particles that result from the outgoing jets plus final-state radiation (see Fig. 1.1). The errors on the (*uncorrected*) data include both statistical and correlated systematic uncertainties. The theory curves are corrected for the track finding efficiency and have an error (*statistical plus systematic*) of around 5%.

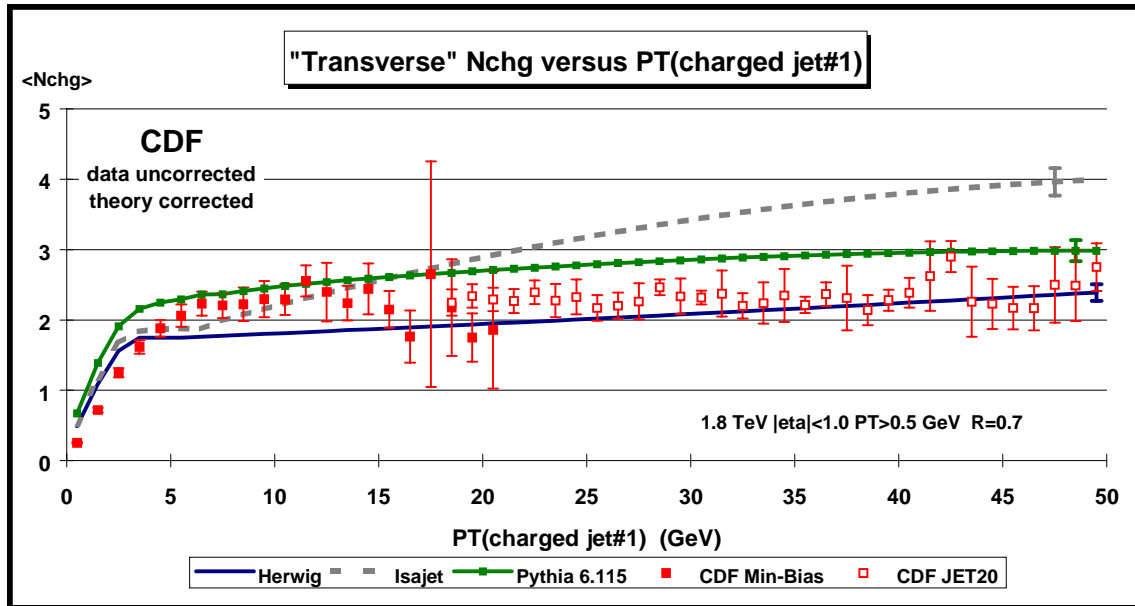


**Fig. 5.1.** Data from Fig.4.9 on the average number of charged particles ( $P_T > 0.5$  GeV and  $|\eta| < 1$ ) as a function of  $P_T(\text{jet\#1})$  (leading charged jet) for the “transverse” region defined in Fig. 4.2 compared with the QCD “hard scattering” Monte-Carlo predictions of Herwig 5.9, Isajet 7.32, and Pythia 6.115. The errors on the (*uncorrected*) data include both statistical and correlated systematic uncertainties. The theory curves are corrected for the track finding efficiency and have an error (*statistical plus systematic*) of around 5%.

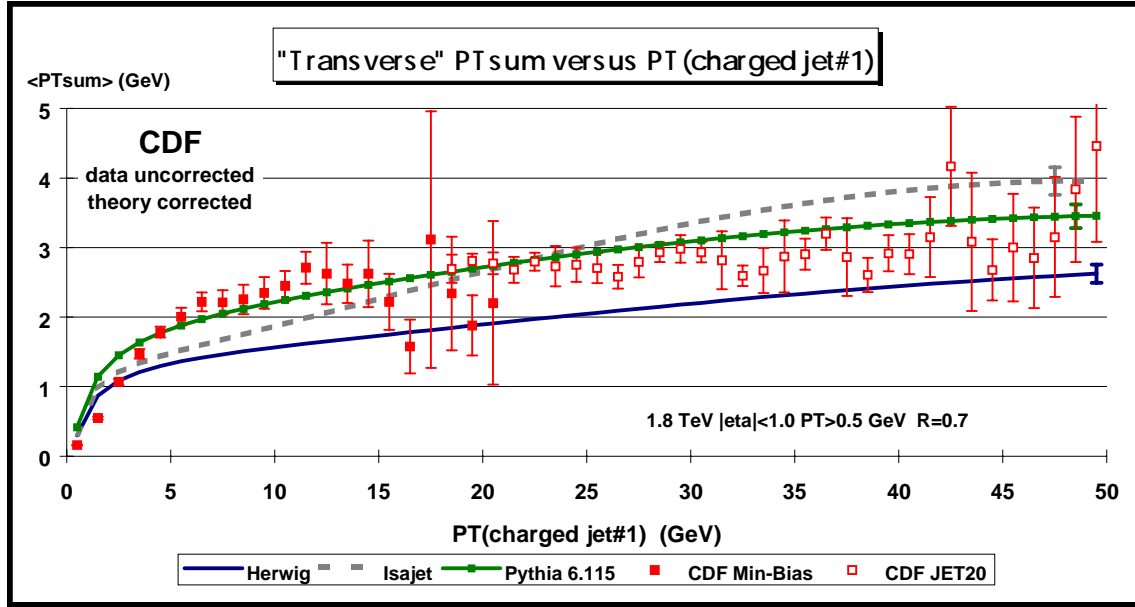


Fig. 5.2. Data from Fig. 4.10 on the average *scalar*  $P_T$  sum of charged particles ( $P_T > 0.5$  GeV and  $|\eta| < 1$ ) as a function of  $P_T(\text{jet\#1})$  (*leading charged jet*) for the “transverse” region defined in Fig. 4.2 compared with the QCD “hard scattering” Monte-Carlo predictions of Herwig 5.9, Isajet 7.32, and Pythia 6.115. The errors on the (*uncorrected*) data include both statistical and correlated systematic uncertainties. The theory curves are corrected for the track finding efficiency and have an error (*statistical plus systematic*) of around 5%.

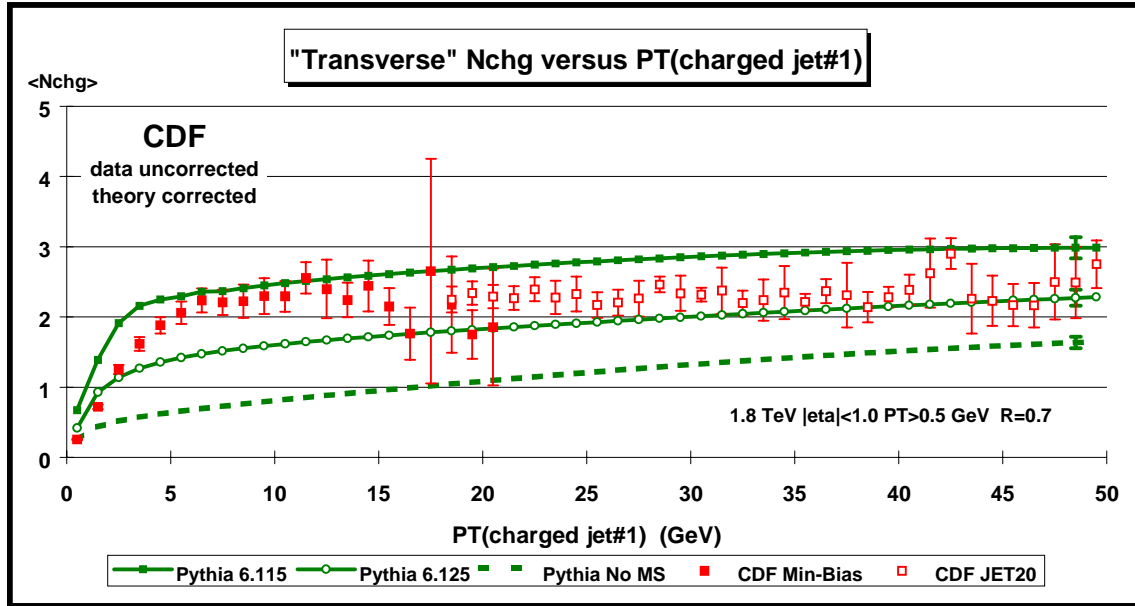


Fig. 5.3. Data from Fig.4.9 on the average number of charged particles ( $P_T > 0.5$  GeV and  $|\eta| < 1$ ) as a function of  $P_T(\text{jet\#1})$  (*leading charged jet*) for the “transverse” region defined in Fig. 4.2 compared with the QCD “hard scattering” Monte-Carlo predictions of Pythia 6.115, Pythia 6.125, and Pythia with no multiple parton scattering (No MS). The errors on the (*uncorrected*) data include both statistical and correlated systematic uncertainties. The theory curves are corrected for the track finding efficiency and have an error (*statistical plus systematic*) of around 5%.

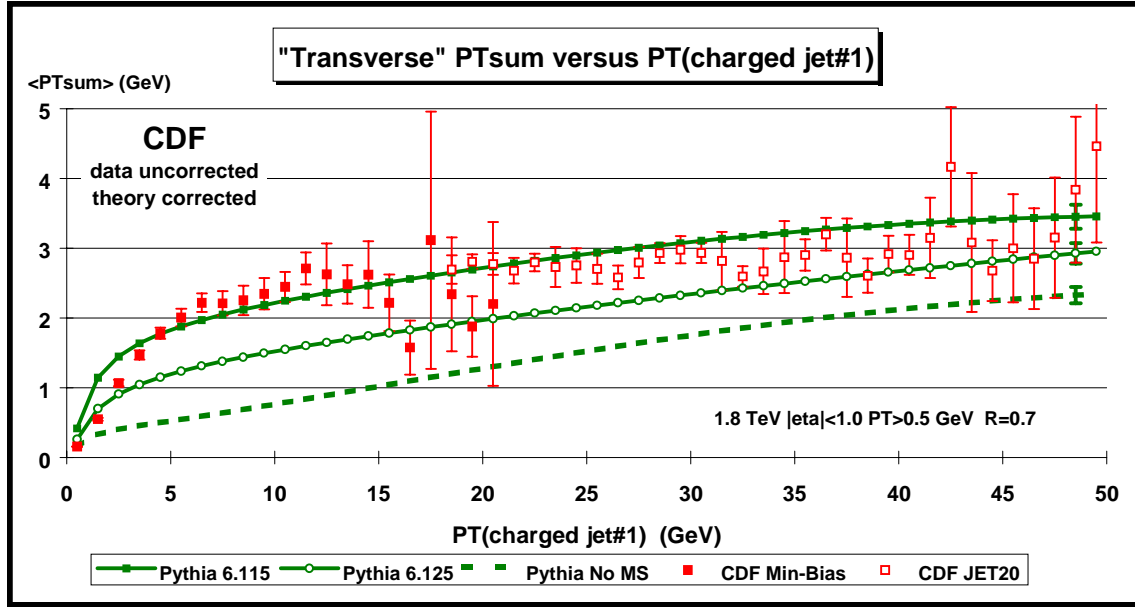


Fig. 5.4. Data from Fig. 4.10 on the average *scalar*  $P_T$  sum of charged particles ( $P_T > 0.5$  GeV and  $|\eta| < 1$ ) as a function of  $P_T(\text{jet\#1})$  (*leading charged jet*) for the “transverse” region defined in Fig. 4.2 compared with the QCD “hard scattering” Monte-Carlo predictions of Pythia 6.115, Pythia 6.125, and Pythia with no multiple parton scattering (No MS). The errors on the (*uncorrected*) data include both statistical and correlated systematic uncertainties. The theory curves are corrected for the track finding efficiency and have an error (*statistical plus systematic*) of around 5%.

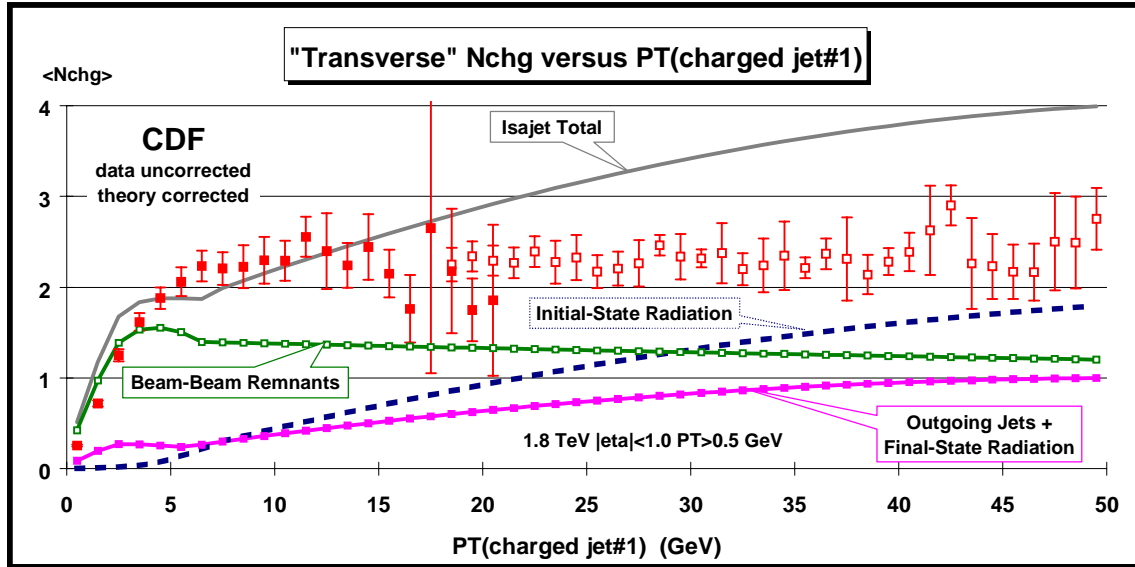
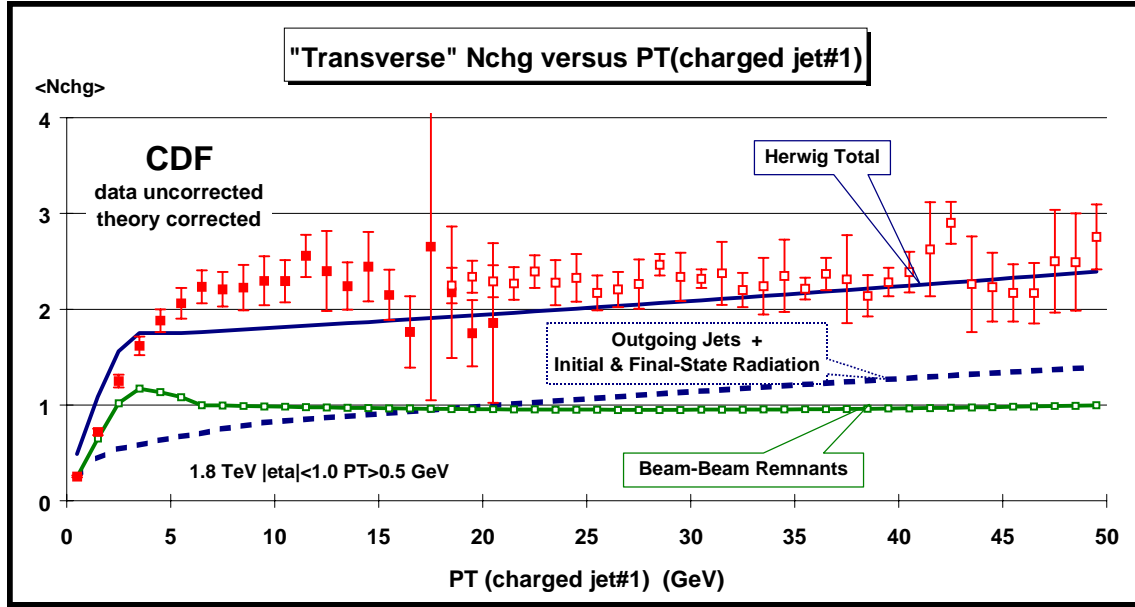
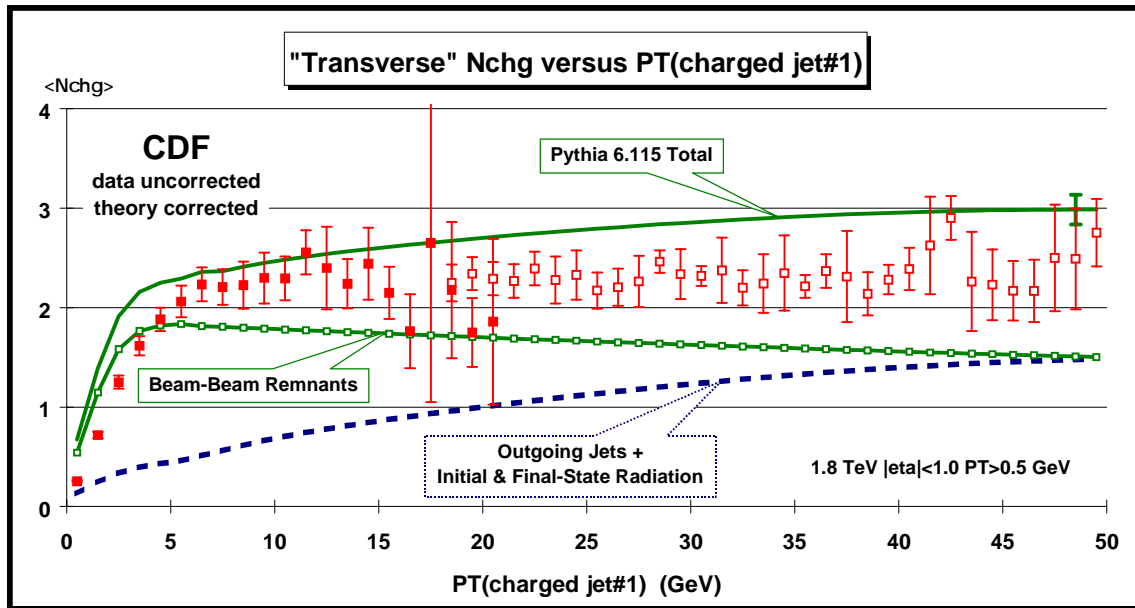


Fig. 5.5. Data from Fig. 4.9 on the average number of charged particles ( $P_T > 0.5$  GeV and  $|\eta| < 1$ ) as a function of  $P_T(\text{jet\#1})$  (*leading charged jet*) for the “transverse” region defined in Fig. 4.2 compared with the QCD “hard scattering” Monte-Carlo predictions of Isajet 7.32. The predictions of Isajet are divided into three categories: charged particles that arise from the break-up of the beam and target (*beam-beam remnants*), charged particles that arise from initial-state radiation, and charged particles that result from the outgoing jets plus final-state radiation (see Fig. 1.1). The errors on the (*uncorrected*) data include both statistical and correlated systematic uncertainties. The theory curves are corrected for the track finding efficiency and have an error (*statistical plus systematic*) of around 5%.



**Fig. 5.6.** Data from Fig. 4.9 on the average number of charged particles ( $P_T > 0.5$  GeV and  $|\eta| < 1$ ) as a function of  $P_T(\text{jet\#1})$  (leading charged jet) for the “transverse” region defined in Fig. 4.2 compared with the QCD “hard scattering” Monte-Carlo predictions of Herwig 5.9. The predictions of Herwig are divided into two categories: charged particles that arise from the break-up of the beam and target (*beam-beam remnants*), and charged particles that result from the outgoing jets plus initial and final-state radiation (*hard scattering component*) (see Fig. 1.1). The errors on the (*uncorrected*) data include both statistical and correlated systematic uncertainties. The theory curves are corrected for the track finding efficiency and have an error (*statistical plus systematic*) of around 5%.



**Fig. 5.7.** Data from Fig. 4.9 on the average number of charged particles ( $P_T > 0.5$  GeV and  $|\eta| < 1$ ) as a function of  $P_T(\text{jet\#1})$  (leading charged jet) for the “transverse” region defined in Fig. 4.2 compared with the QCD “hard scattering” Monte-Carlo predictions of Pythia 6.115. The predictions of Pythia are divided into two categories: charged particles that arise from the break-up of the beam and target (*beam-beam remnants*), and charged particles that result from the outgoing jets plus initial and final-state radiation (*hard scattering component*). For Pythia the beam-beam remnants include contributions from multiple parton scattering (see Fig. 1.2). The errors on the (*uncorrected*) data include both statistical and correlated systematic uncertainties. The theory curves are corrected for the track finding efficiency and have an error (*statistical plus systematic*) of around 5%.

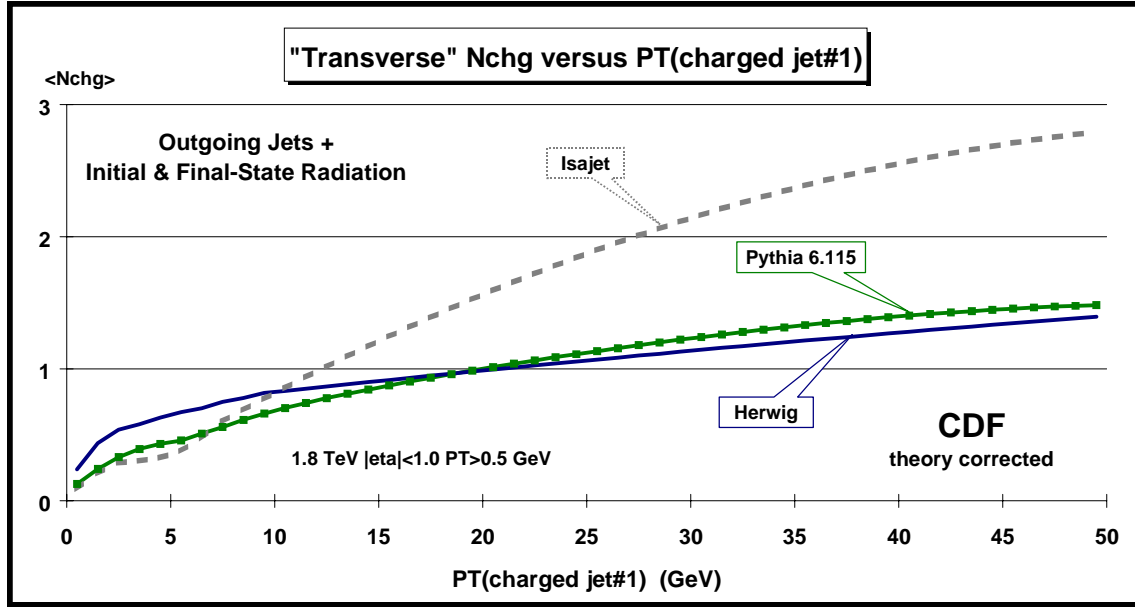


**Fig. 5.8.** QCD “hard scattering” Monte-Carlo predictions from Herwig 5.9, Isajet 7.32, and Pythia 6.115 of the average number of charged particles ( $P_T > 0.5$  GeV and  $|\eta| < 1$ ) as a function of  $P_T(\text{jet\#1})$  (leading charged jet) for the “transverse” region defined in Fig. 4.2 arising from the outgoing jets plus initial and final-state radiation (hard scattering component). The curves are corrected for the track finding efficiency and have an error (statistical plus systematic) of around 5%.

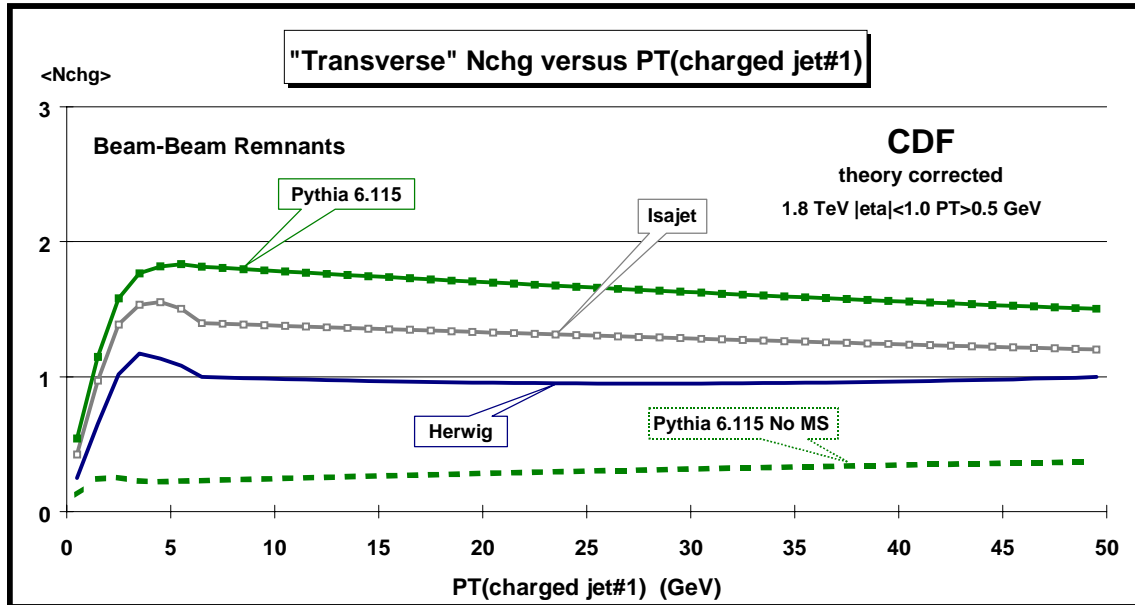


**Fig. 5.9.** QCD “hard scattering” Monte-Carlo predictions from Herwig 5.9, Isajet 7.32, Pythia 6.115, and Pythia with no multiple parton scattering (No MS) of the average number of charged particles ( $P_T > 0.5$  GeV and  $|\eta| < 1$ ) as a function of  $P_T(\text{jet\#1})$  (leading charged jet) for the “transverse” region defined in Fig. 4.2 arising from the break-up of the beam and target (beam-beam remnants). For Pythia the beam-beam remnants include contributions from multiple parton scattering (see Fig. 1.2). The curves are corrected for the track finding efficiency and have an error (statistical plus systematic) of around 5%.

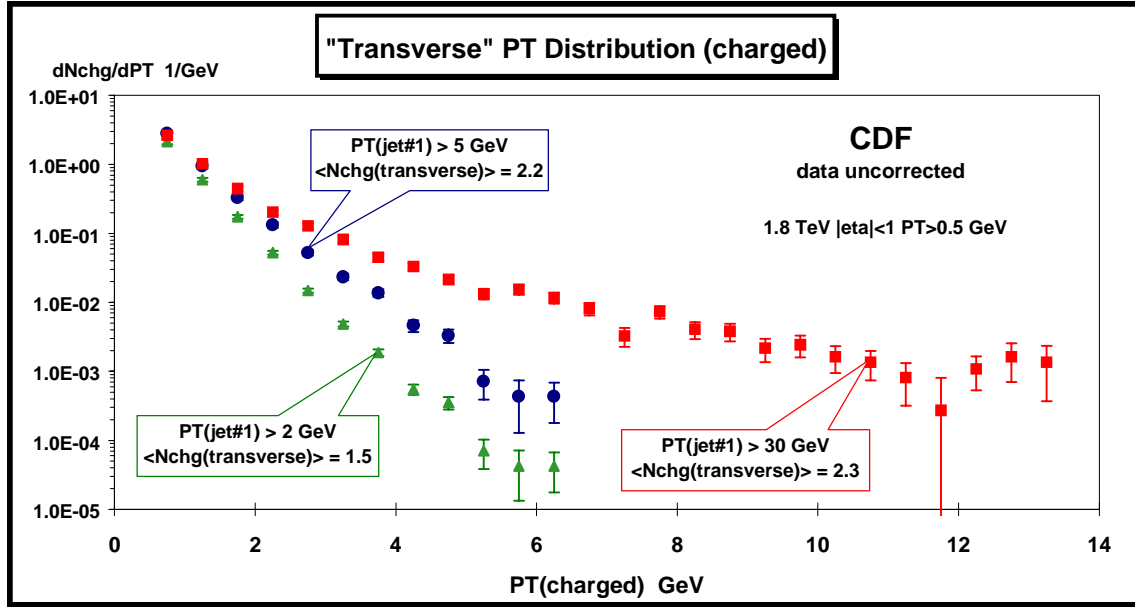


**Fig. 5.10.** Data on the transverse momentum distribution of charged particles ( $P_T > 0.5$  GeV and  $|\eta| < 1$ ) in the “transverse” region defined in Fig. 4.2 for  $P_{T(\text{jet}\#1)} > 2, 5$ , and  $30$  GeV, where jet#1 is the leading charge particle jet. The  $P_{T(\text{jet}\#1)} > 2$  and  $5$  GeV points are Min-Bias data and the  $P_{T(\text{jet}\#1)} > 30$  GeV are JET20 data. Each point corresponds to the charge particle density  $dN_{\text{chg}}/dP_T$  and the integral of the distribution gives the average number of charged particles in the “transverse” region,  $\langle N_{\text{chg}}(\text{transverse}) \rangle$ . The errors on the (*uncorrected*) data include both statistical and correlated systematic uncertainties. (Note the *logarithmic scale* on the vertical axis.)

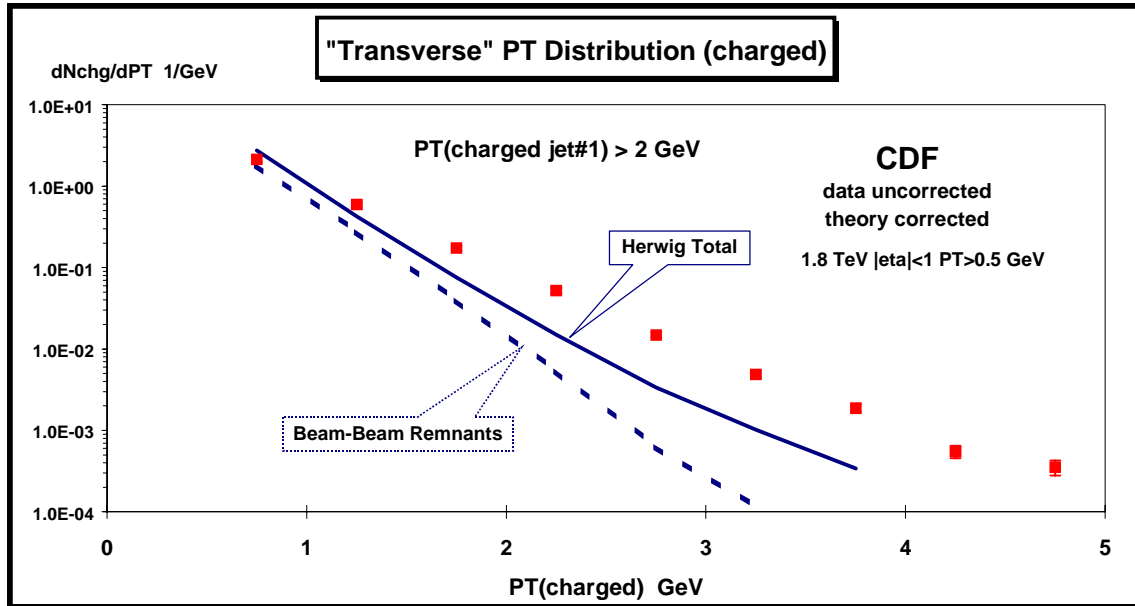


**Fig. 5.11.** Data from Fig. 5.10 on the transverse momentum distribution of charged particles ( $P_T > 0.5$  GeV and  $|\eta| < 1$ ) in the “transverse” region defined in Fig. 4.2 for  $P_{T(\text{jet}\#1)} > 2$  GeV compared to the QCD “hard scattering” Monte-Carlo predictions from Herwig 5.9. The dashed curve shows the contribution arising from the break-up of the beam and target (*beam-beam remnants*) predicted by Herwig. The errors on the (*uncorrected*) data include both statistical and correlated systematic uncertainties. The theory curves are corrected for the track finding efficiency and have an error (*statistical plus systematic*) of around 5%.

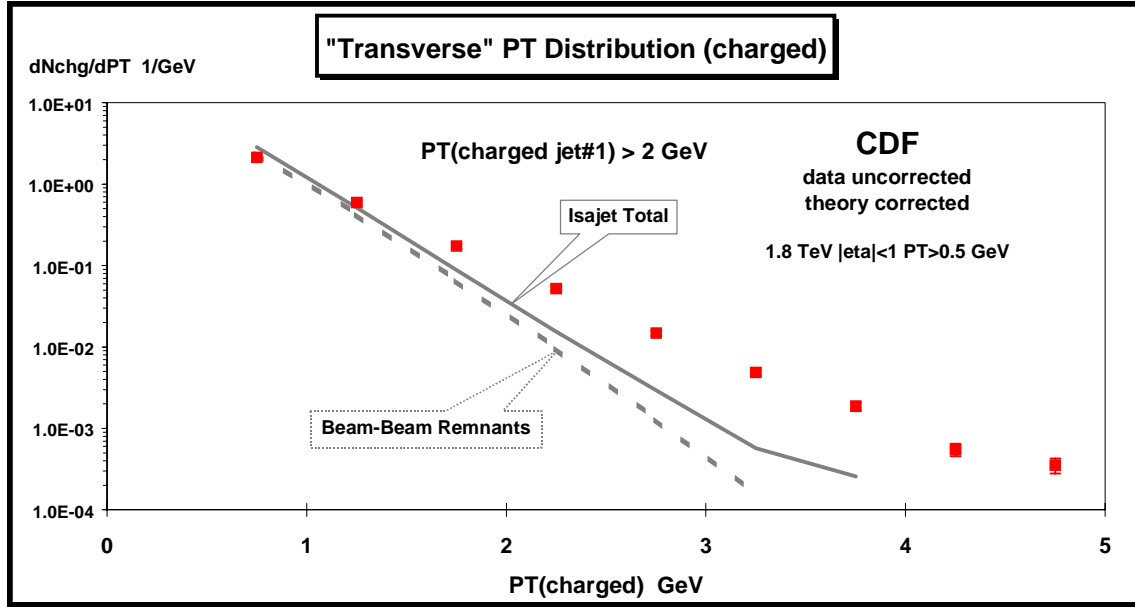


**Fig. 5.12.** Data from Fig. 5.10 on the transverse momentum distribution of charged particles ( $P_T > 0.5$  GeV and  $|\eta| < 1$ ) in the “transverse” region defined in Fig. 4.2 for  $P_{T(\text{jet}\#1)} > 2$  GeV compared to the QCD “hard scattering” Monte-Carlo predictions from Isajet 7.32. The dashed curve shows the contribution arising from the break-up of the beam and target (*beam-beam remnants*) predicted by Isajet. The errors on the (*uncorrected*) data include both statistical and correlated systematic uncertainties. The theory curves are corrected for the track finding efficiency and have an error (*statistical plus systematic*) of around 5%.

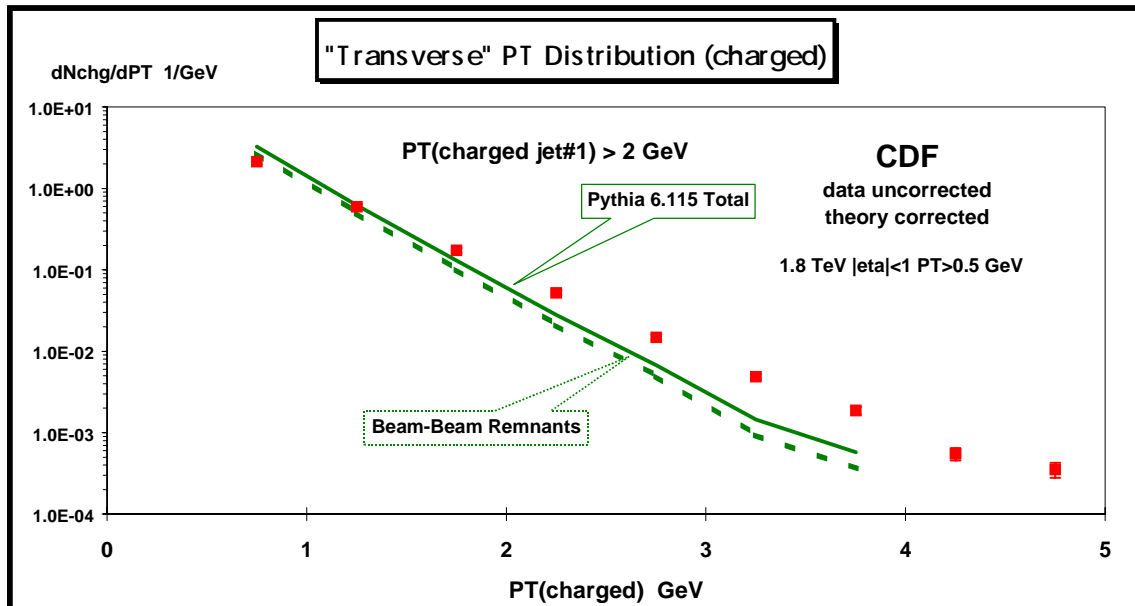


**Fig. 5.13.** Data from Fig. 5.10 on the transverse momentum distribution of charged particles ( $P_T > 0.5$  GeV and  $|\eta| < 1$ ) in the “transverse” region defined in Fig. 4.2 for  $P_{T(\text{jet}\#1)} > 2$  GeV compared to the QCD “hard scattering” Monte-Carlo predictions from Pythia 6.115. The dashed curve shows the contribution arising from the break-up of the beam and target (*beam-beam remnants*) predicted by Pythia. For Pythia the beam-beam remnants include contributions from multiple parton scattering (see Fig. 1.2). The errors on the (*uncorrected*) data include both statistical and correlated systematic uncertainties. The theory curves are corrected for the track finding efficiency and have an error (*statistical plus systematic*) of around 5%.

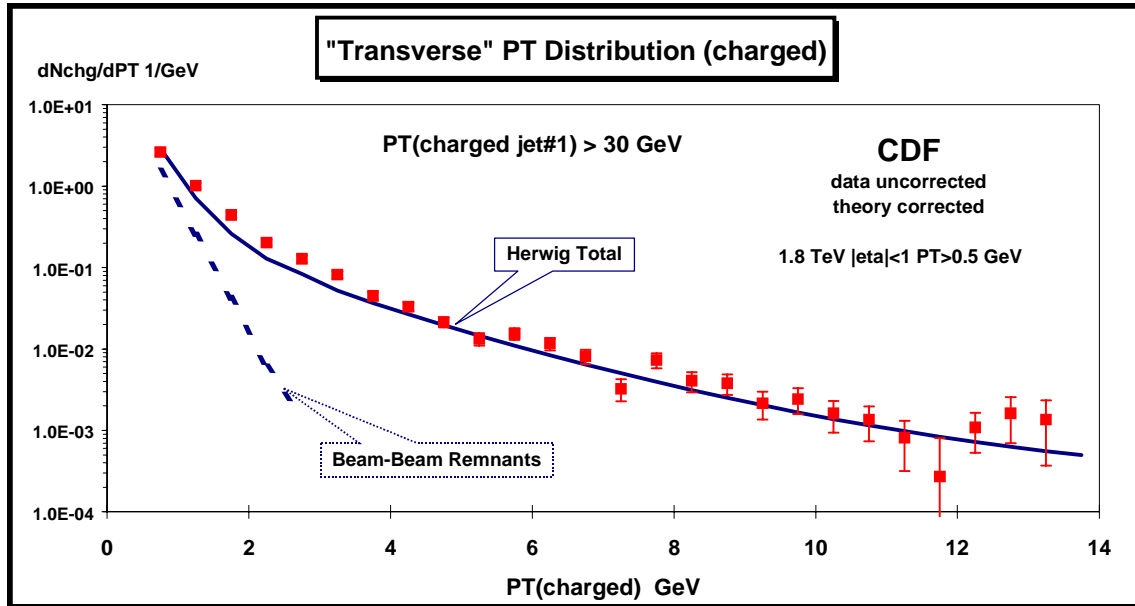


**Fig. 5.14.** Data from Fig. 5.10 on the transverse momentum distribution of charged particles ( $P_T > 0.5$  GeV and  $|\eta| < 1$ ) in the “transverse” region defined in Fig. 4.2 for  $P_{T(\text{jet}\#1)} > 30$  GeV compared to the QCD “hard scattering” Monte-Carlo predictions from Herwig 5.9. The dashed curve shows the contribution arising from the break-up of the beam and target (*beam-beam remnants*) predicted by Herwig. The errors on the (*uncorrected*) data include both statistical and correlated systematic uncertainties. The theory curves are corrected for the track finding efficiency and have an error (*statistical plus systematic*) of around 5%.

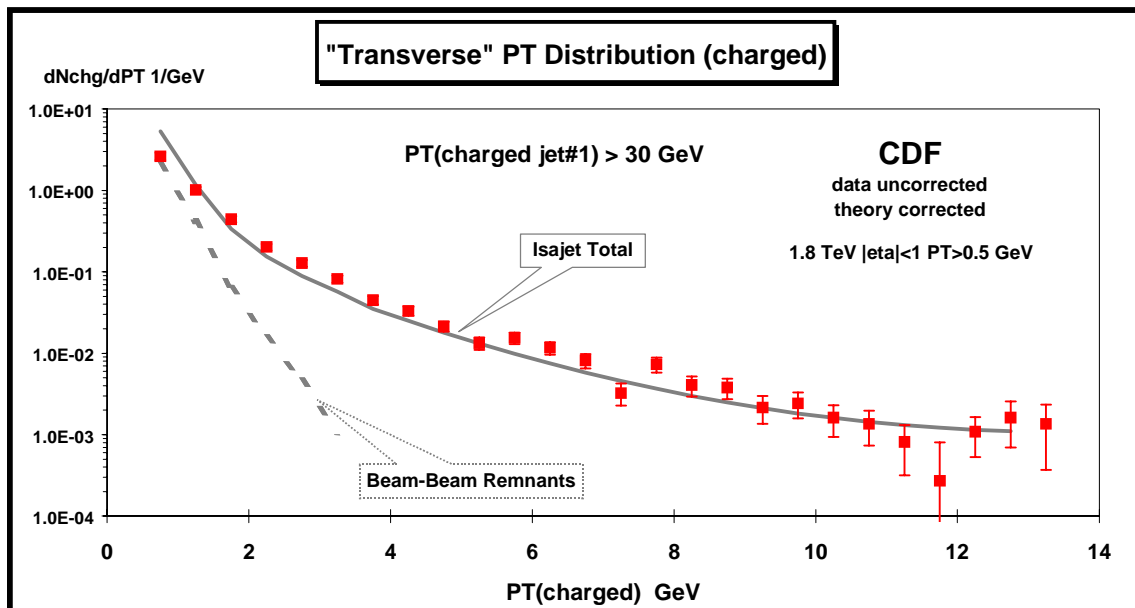


**Fig. 5.15.** Data from Fig. 5.10 on the transverse momentum distribution of charged particles ( $P_T > 0.5$  GeV and  $|\eta| < 1$ ) in the “transverse” region defined in Fig. 4.2 for  $P_{T(\text{jet}\#1)} > 30$  GeV compared to the QCD “hard scattering” Monte-Carlo predictions from Isajet 7.32. The dashed curve shows the contribution arising from the break-up of the beam and target (*beam-beam remnants*) predicted by Isajet. The errors on the (*uncorrected*) data include both statistical and correlated systematic uncertainties. The theory curves are corrected for the track finding efficiency and have an error (*statistical plus systematic*) of around 5%.

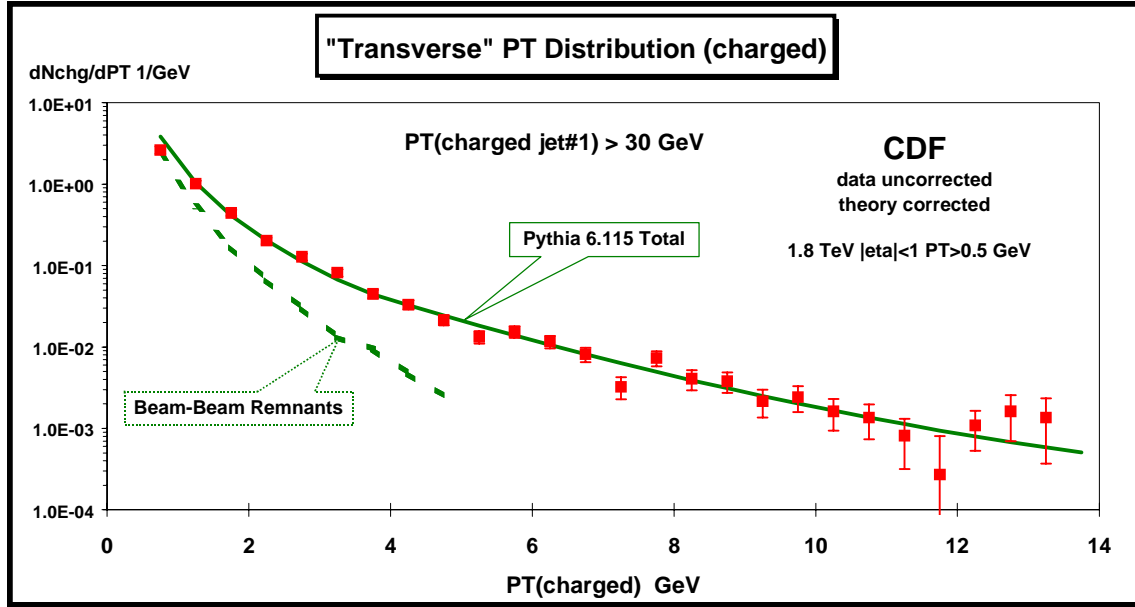


**Fig. 5.16.** Data from Fig. 5.10 on the transverse momentum distribution of charged particles ( $P_T > 0.5 \text{ GeV}$  and  $|\eta| < 1$ ) in the “transverse” region defined in Fig. 4.2 for  $P_{T(\text{jet\#1})} > 30 \text{ GeV}$  compared to the QCD “hard scattering” Monte-Carlo predictions from Pythia 6.115. The dashed curve shows the contribution arising from the break-up of the beam and target (*beam-beam remnants*) predicted by Pythia. For Pythia the beam-beam remnants include contributions from multiple parton scattering (see Fig. 1.2). The errors on the (*uncorrected*) data include both statistical and correlated systematic uncertainties. The theory curves are corrected for the track finding efficiency and have an error (*statistical plus systematic*) of around 5%.